Three-Dimensional Kinematic and Microphysical Evolution of Florida Cumulonimbus. Part III: Vertical Mass Transport, Mass Divergence, and Synthesis

SANDRA E. YUTER AND ROBERT A. HOUZE JR.

Department of Atmospheric Sciences, University of Washington, Seattle, Washington

(Manuscript received 31 March 1994, in final form 30 November 1994)

ABSTRACT

A statistical technique is employed to examine the evolving properties of the ensemble small-scale variability of high-resolution radar data collected in a multicellular Florida thunderstorm. This paper examines vertical mass transport and mass divergence and synthesizes these observations with results from the first two parts of the study into a self-consistent conceptual model that describes the convective-to-stratiform transition of the storm.

Vertical mass transport distributions indicate that the more numerous weak and moderate-strength upward and downward velocities, not the few strongest, accomplished most of the vertical mass transport in the storm. Hence, most of the mass of precipitation is condensed outside the areas of intense upward motion. These data thus suggest a change in the way we think about convection. Although the few regions of strongest vertical motion play a part in the overall storm evolution by dispersing particles throughout the depth of the storm, it is the more prevalent weak and moderate-strength upward velocities that are the more important determinants of the precipitation processes.

An extension of bubble-based conceptual models of convection is proposed to account for the convective-to-stratiform transition. Bubbles of positively buoyant air produced at low levels are weakened by varying amounts of entrainment and slowed down by pressure gradient forces as they rise. Thus many bubbles are slowed and stopped at mid- and upper levels. The weakened parcels flatten, encompass more area and, in the process, laterally spread their associated hydrometeors. As the weak updraft parcels congregate at mid- and upper levels of the storm, they create the region of weak mean ascent that is characteristic of stratiform mean vertical velocity profiles. Below the 0°C level, precipitation-associated downdrafts dominate the ensemble of smaller-scale drafts and create mean weak descent at low levels.

1. Introduction

This paper is the third of a three-part study (the preceding papers, Yuter and Houze 1995a,b, are referred to as YH Part I and YH Part II) that addresses the evolution of cumulonimbus and focuses on the convective-to-stratiform transition of a multicellular thunderstorm. The purpose of this study is to shed light on how the convective-to-stratiform transition is accomplished. High-resolution radar data observations made on 15 August 1991 during the Convection and Precipitation Electrification Experiment (CaPE) project in east central Florida are the primary data for this study. (The experimental setting and weather situation for the 15 August 1991 storm under study are described in YH Part I.) A statistical tool introduced in YH Part II, called a contoured frequency by altitude diagram (CFAD), aids in the analysis of radar data volumes by displaying the distribution with height of the ensemble small-scale variability of several observed and derived variables.

The character of precipitating convective clouds changes as a storm evolves (Battan 1973; Houze 1977; Zipser 1977). The stages of storm evolution are called *convective, transition* or *intermediary,*[1] and *stratiform*[2] (Houze 1993, chapters 6 and 9). Figure 1 conceptualizes the sequence of events seen in radar reflectivity vertical cross sections as a convective region evolves into a stratiform region. If there is low or no vertical wind shear in the environment, the decay of a succession of groups of convective cells leads to the formation of a stratiform region. Precipitation-size ice particles carried rapidly upward in the growing convective cells settle out as the vertical air motions in the cells weaken; the trajectory of each particle is vertically downward in the coordinate system moving with the cloud. The radar reflectivity then takes on a stratiform structure, with a bright band at the melting layer. A structure similar to that in Fig. 1c can also occur in strong shear, in which case positions 3, 2, and 1 indicate successive points along the trajectory

Corresponding author address: Sandra E. Yuter, Department of Atmospheric Sciences, University of Washington, Box 351640, Seattle, WA 98195.

[1] *Transition* and *intermediary* are terms that describe a region or stage of the storm between convective and stratiform (Biggerstaff and Houze 1991, 1993; Houze 1993; Mapes and Houze 1993; Braun and Houze 1994). See YH Part I, section 2 for further explanation).

[2] *Stratiform* is defined in terms of the vertical velocity structure such that $0 < |w| \ll V_t$, where w is the vertical air velocity and V_t is the fall speed of precipitation particles (see YH Part I, section 2 or Houze 1993, chapter 6 for further explanation).

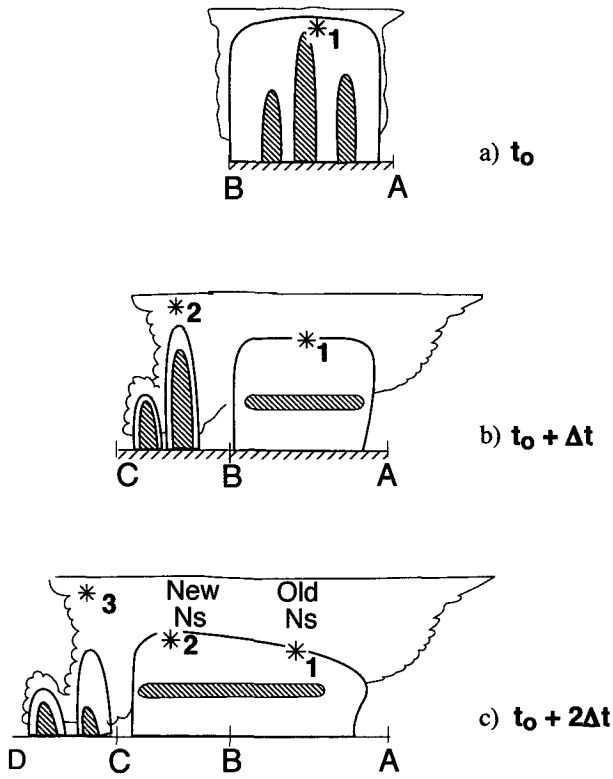

FIG. 1. Conceptual model of the development of nimbostratus (Ns) associated with deep convection in a coordinate system moving with the clouds. Panels (a), (b), and (c) show vertical cross sections through a developing storm at three sequential times. Radar echo boundary is indicated by heavy line and strong echo is indicated by hatched areas. The visible cloud boundary is sketched. Asterisks trace the fallout of three ice particles. Letters correspond to storm relative positions. Adapted from Leary and Houze (1979) and Houze (1993).

of a single particle that is transported left to right while falling (Houze 1993, 211–213).

The shapes of mean vertical profiles of radar reflectivity, vertical velocity, and divergence grossly characterize the stages of storm evolution (Fig. 2). We refer to these mean vertical profiles in order to tie our results back to those of previous studies. We gain new insights by interpreting the evolution in the shape of such mean vertical profiles in terms of the evolving statistical distributions for the entire storm. [As discussed in YH Part II, the shapes of vertical profiles of the mean vertical air motions and radar reflectivity characteristics in convective and stratiform regions are roughly consistent across different storms in different regimes. To illustrate the typical shapes of these profiles in convective and stratiform regions, examples from the well-documented 10–11 June 1985 PRE-STORM[3] case observed in Kansas are used (Rutledge et al. 1988; Biggerstaff and Houze 1991).]

YH Part II analyzes the evolution of mean profiles of reflectivity (Fig. 2a). In this paper, we further analyze the kinematic evolution of the storm as represented by typical profiles of mean vertical velocity and divergence in convective and stratiform regions (Figs. 2b and 2c). The profile of mean vertical velocity (Fig. 2b, solid line) from a convective region typically shows positive values of w for all heights, with a midlevel maximum. In contrast, the stratiform profile of mean vertical velocity (Fig. 2b, dashed line) is weaker overall and characterized by mean descent below the environmental 0°C level and mean ascent above. The mean mass divergence profile undergoes a related evolution (Fig. 2c). Mean vertical profiles of mass divergence in convection (Fig. 2c, solid line) exhibit convergence at low levels, with the peak convergence el-

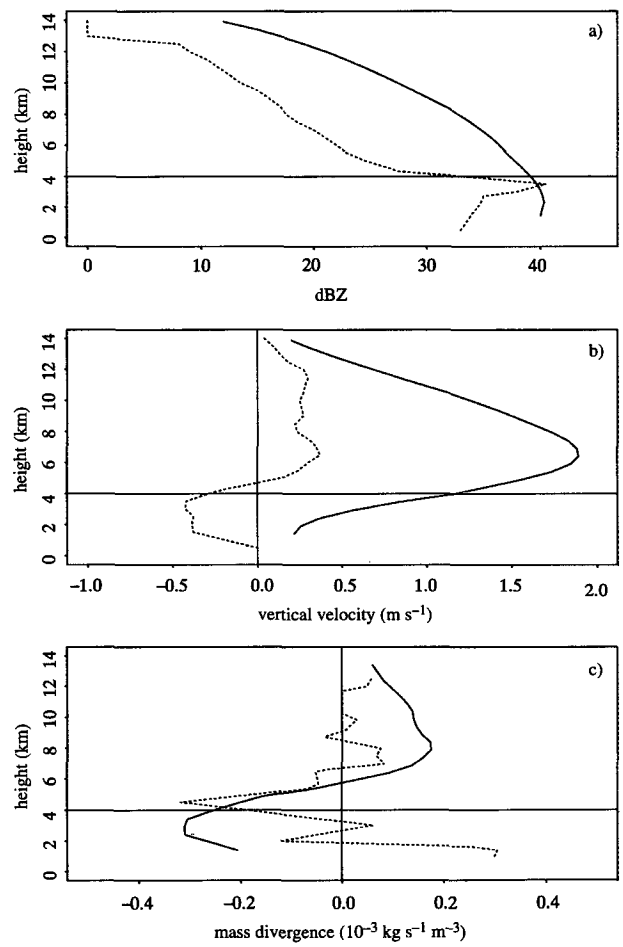

FIG. 2. Characteristic mean profiles of vertical velocity and mass divergence in convection (solid line) and stratiform (dashed line) regions in the 10–11 June 1985 mesoscale convective system observed in Kansas during the PRE-STORM project. (a) Mean reflectivity, (b) vertical velocity, (c) mass divergence adapted from Rutledge et al. (1988). Horizontal line at 4 km indicates the 0°C level. Data for (a) and (b) provided by S. Braun.

[3] Oklahoma–Kansas Preliminary Regional Experiment for the Stormscale Operational and Research Program—Central Phase (Cunning 1986).

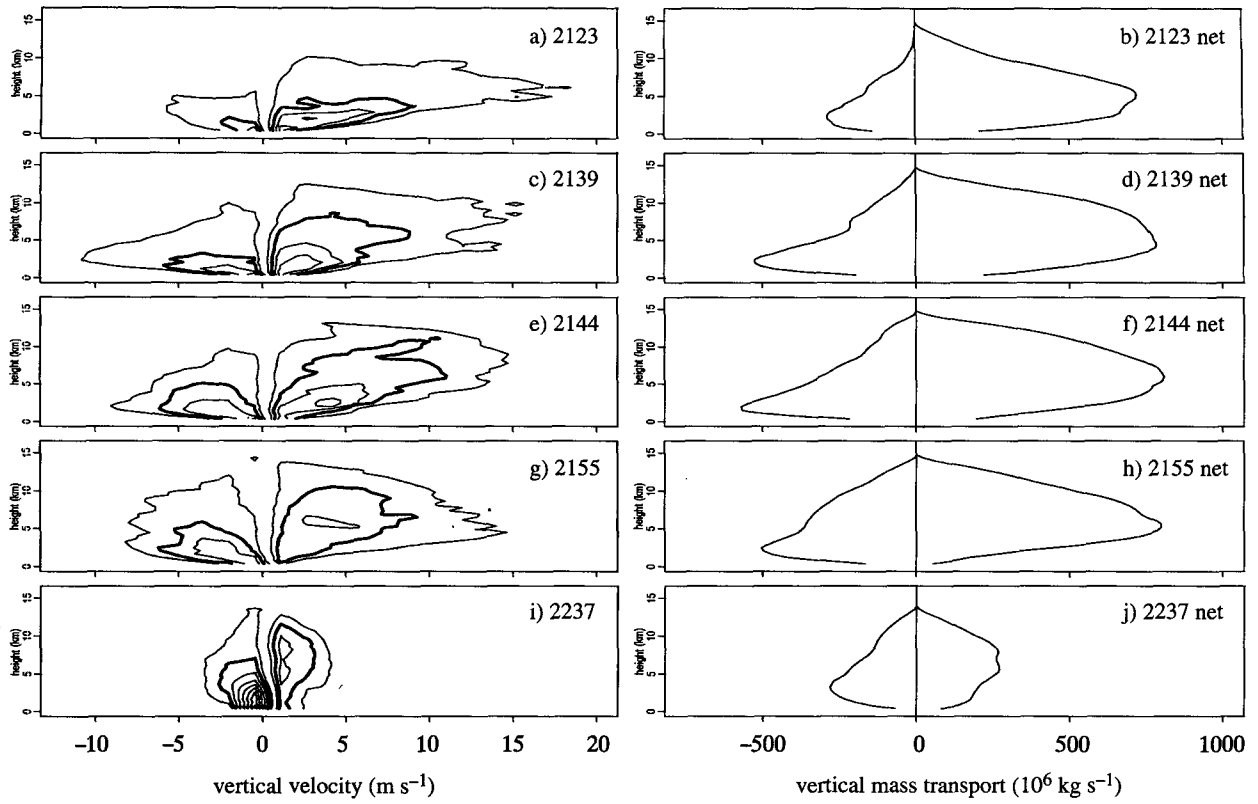

FIG. 3. Time series of vertical-mass-transport-weighted CFADs of vertical velocity (left column) and net vertical mass transport upward and downward (right column). Vertical mass transport is contoured in the CFADs at 25 × 10^6 kg s^{-1} intervals and the ±50 × 10^6 kg s^{-1} contours are highlighted. One-meter-per-second bins are used in construction of CFAD.

evated above the surface. Convergence weakens above this peak and the profile becomes divergent at mid- and upper levels. The characteristic stratiform mass divergence profile (Fig. 2c, dashed line) is divergent at the surface, has a relatively strong peak in convergence near the 0°C level, and is divergent at upper levels. The first objective of this part of the study is to understand how the kinematic structure of a storm evolves from a state represented by the convective curves to that represented by the stratiform curves in Fig. 2. We approach this problem by examining the ensemble small-scale variability of the vertical mass transport and horizontal mass divergence (sections 2–4). Our second objective is to integrate the results of YH Parts I–III into a model of the self-consistent mechanisms by which the characteristic observed properties of reflectivity, differential reflectivity, vertical velocity, vertical mass transport, and horizontal mass divergence within the entire storm evolve from their convective to stratiform states (section 5).

2. Vertical mass transport

The vertical mass transport of air differs from the vertical velocity in that vertical velocity indicates how rapidly the air is moving while vertical mass transport (kg s^{-1}) indicates how much air is moved and, therefore, how much water is condensed, which is key to understanding precipitation processes.

a. *Mass-transport-weighted CFADs of vertical velocity*

Information on the vertical transport of mass is inherently present in the CFADs of vertical velocity (Fig. 3 of YH Part II); however, it is not easy to see in those plots since they are dominated by vertical velocities close to zero, which have little effect on the mass transport. This fact led us to plot CFADs of the mass-transport-weighted vertical velocity[4] (Figs. 3 and 4). These plots are similar to the CFADs of vertical velocity except for the value that is contoured. In the case of the vertical-mass-transport-weighted CFADs of vertical velocity, the contours are of the vertical mass transport of air (M_{ij}), accounted for by all the drafts where $w_i \leq w \leq w_i + \Delta w$ within the height interval $z_j \leq z \leq z_j + \Delta z$. This quantity is expressed as

[4] The presentation of the vertical mass transport data via a contoured frequency by altitude diagram is similar to the spectral distributions of mass flux used by Tao et al. (1987) to present results from a three-dimensional numerical cloud ensemble model.

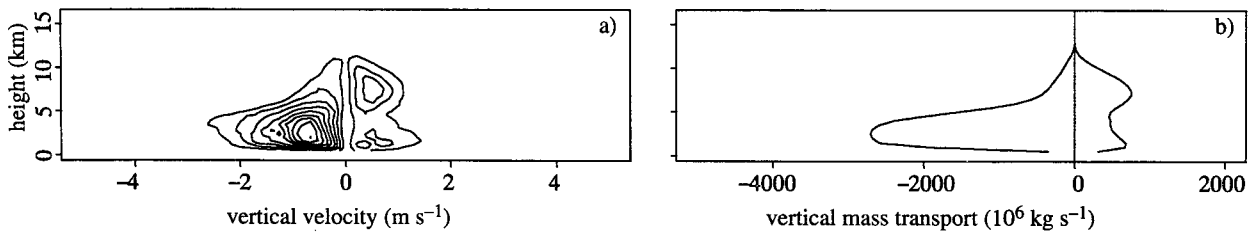

FIG. 4. Vertical-mass-transport-weighted CFAD of vertical velocity (a) and net vertical mass transport upward and downward (b) from a stratiform volume observed to the rear of a Kansas squall line at 0345 UTC 11 June 1985 during the PRE-STORM project. CFAD bin size for $w = 0.2$ m s^{-1}, contoured at 50×10^6 kg s^{-1} intervals.

$$M_{ij} = \int_{w_i}^{w_i+\Delta w} \int_{z_j}^{z_j+\Delta w} \frac{\partial^2 N(w, z)}{\partial z \partial w} w \rho a dw dz, \qquad (1)$$

where N is the frequency distribution function defined such that $[\partial^2 N(w, z)/\partial z \partial w] dz dw$ is the number of observations of vertical velocity in the range w to $w + dw$ at heights z to $z + dz$, ρ is the density of air, and a is the horizontal area of the Cartesian grid element (0.25 km^2).

In Fig. 3, a contour interval of 25×10^6 kg s^{-1} is used to bring out the pattern of vertical mass transport topography and the 50×10^6 kg s^{-1} and -50×10^6 kg s^{-1} contours are highlighted to emphasize the regions of large mass transport upward and downward. These plots permit easy comparison of the vertical mass transport contributed by drafts of a particular magnitude at different levels and vertical mass transport contributed by drafts of different magnitudes at the same level. The changing pattern of the distribution of vertical mass transport with time reveals the evolution of mass transport within the storm. Note that since the contoured field is not normalized by the number of data points, the values for the contours are dependent on the size of the volume containing the data.

The net (or total) mass transport for updrafts and downdrafts at each level M_{Tj} is shown in the right column of Figs. 3 and 4. These were computed according to

$$M_{Tj} = \sum_k w_k \rho(z_j) a, \qquad (2)$$

where k is an index to grid points with vertical velocity values in the x–y plane. The units of M_{Tj} are kilograms per second, and the summation has been done separately for positive and negative vertical velocity. In Figs. 3b,d, f ,h, j, and 4b, the area between the net positive (negative) vertical mass transport curve and the z axis is proportional to the net upward (downward) mass transport for the storm.

Since M_{Tj} is proportional to density, area, and vertical velocity, the profiles of net vertical mass transport M_{Tj} (Figs. 3b,d,f,h,j, and 4b) are helpful in quantifying only certain gross characteristics of vertical mass transport, such as: Was more air going up than down? At what levels was the most air moving? And how did the net mass transport change as the storm evolved? They do not distinguish *what magnitudes of drafts* were producing the vertical mass transport.

The vertical-mass-transport-weighted CFADs of vertical velocity M_{ij} (Figs. 3a,c,e,g,i, and 4a) distinguish several factors contributing to net vertical mass transport. The left-to-right variation of the vertical mass transport distribution topography in the CFAD shows the frequency distribution of vertical velocity producing the mass transport. The up-and-down-the-page variation of the vertical mass transport distribution in the CFAD shows the distribution of updrafts and downdrafts with height. The amplitude of the topography shown by the contours in the CFAD shows the growing area of the storm (increasing number of points) at each level. The changes in these aspects of the statistical distribution of vertical mass transport shown by Figs. 3 and 4 are important clues that we use below to decipher changes associated with the storm's convective-to-stratiform transition.

b. *Distribution of vertical mass transport in the storm*

1) DOMINATION OF MODERATE VERTICAL VELOCITIES

The spacing and location of the contours in the vertical-mass-transport-weighted CFADs of vertical velocity (Fig. 3) indicate that the valleys (strong downward mass transport, inside the -75×10^6 kg s^{-1} contour) and the peaks (strong upward mass transport, inside 75×10^6 kg s^{-1} contour) in the vertical-mass-transport distribution topography were produced almost entirely by downward velocities between -1 and -5 m s^{-1} and upward velocities between 1 and 6 m s^{-1}. Thus—in a manner analogous to the middle-income tax burden—the majority of the mass transport in the volume was produced primarily by velocities of moderate strength. The many points close to zero vertical velocity (the low-income bracket) could not contribute much to the mass transport (tax revenue) despite their large numbers. The strong (absolute value greater than 10 m s^{-1}) upward and downward velocities (the high-income bracket), although they produced strong mass transport individually (large tax payments), were not numerous enough to make a large

contribution to the net. This left the moderate strength velocities (the middle-income bracket) to carry the burden of moving the majority of mass around in the storm. Thus, *the strongest upward velocities (> 10 m s^{-1}) were not the primary agents in the upward vertical transport of mass in the storm. As a result, most of the condensation occurred outside the regions of the most intense upward motion.*

2) Evolution of net vertical mass transport interpreted via CFADs

In the convective stages of the storm, net upward mass transport exceeded net downward mass transport at all levels (Figs. 3b,d,f,h). Net downward mass transport was greatest at low levels and net upward mass transport was greatest at midlevels. The maximum net downward mass transport at a level (-570×10^6 kg s^{-1} at the 2-km altitude) occurred at 2144 UTC (Fig. 3f), the same time as the maximum net upward mass transport at a level (808×10^6 kg s^{-1} at the 6-km altitude). As the storm aged further, the magnitude of total upward and downward mass transports for the storm decreased. The difference between the net upward and net downward mass transports in the storm became smaller, until at the intermediary stage (as defined in YH Part I, section 2), net upward and net downward vertical mass transports were of nearly equal magnitude, though the peaks were offset in height (2237 UTC, Fig. 3j).

During the early convective stages of the storm (2123 and 2139 UTC, Figs. 3b,d), the net downward mass transport increased at every level. At both 2123 and 2139, the shape of the downward mass transport distribution topography (Figs. 3a,c) was characterized by a sharp peak at the lowest levels corresponding to vertical velocities near -1 m s^{-1}. The downward mass transport from downdrafts stronger than -5 m s^{-1} and the overall magnitude of the contours of the topography increased between 2123 and 2139 (Figs. 3a,c). The increase in net downward mass transport can be related both to an increase in the area of the storm at each level and the development of a few strong downdrafts at low levels.

The total upward mass transport also increased at each level between 2123 and 2139 (Figs. 3b and 3d). The upward mass transport distribution topography was concentrated below 5 km (Fig. 3a), and the peak upward mass transport was centered near the 1-km altitude and associated with updrafts of 1 m s^{-1}. As the storm grew (2139 UTC), the peak upward mass transport remained centered near 1 km and 1 m s^{-1} vertical velocity (Fig. 3c). Between 2123 and 2139, the contours of upward mass transport had spread apart in the vertical while remaining in roughly similar positions in the horizontal (Figs. 3a,c). Increases in the magnitudes of the upward mass transport distribution topography (Fig. 3c) at all levels (i.e., increased areal coverage, Fig. A1 of YH Part II) contributed to the increase in net upward transport (Fig. 3d). The changes in the distribution of positive vertical velocity occurring above 10 km between 2123 and 2139 (Figs. 3b,d of YH Part II) had a relatively small effect on upward mass transport (Figs. 3a,c). Thus, it was likely that an increase in the area of the storm at all levels was the primary source of the increased net upward mass transport between 2123 and 2139.

At 2144 UTC, the outlier contour (-25×10^6 kg s^{-1}) of the downward mass transport distribution topography moved inward toward lower downdraft magnitudes (Fig. 3e). Otherwise, the downward mass transport topography remained concentrated at low levels and at weak vertical velocity. Despite the decreasing contribution from extreme downdrafts ($w < -8$ to -10 m s^{-1}), the increase in the frequency of moderate downdrafts of about -2 to -4 m s^{-1} (Fig. 3h of YH Part II) was sufficient to maintain the net downward mass transport at each level (Fig. 3f) to values close to or greater than those occurring at 2139 (Fig. 3d).

At the time of most vigorous convective activity in the storm (2144 UTC), most of the upward mass transport was still from the weaker velocities (<5 m s^{-1}) and at lower levels (Fig. 3e). The increase of total upward mass transport at upper levels (Fig. 3f) is seen from the CFADs of mass transport in Fig. 3e to have been due to the increased frequency of stronger upward velocities at upper levels, which were also seen in the outliers of the frequency distribution of vertical velocity (Fig. 3f of YH Part II). The overall peak in upward mass transport, however, remained at lower levels and was associated with updrafts of moderate strength. This low-level maximum had shifted to a slightly higher altitude (2.5 km), and its topography had become less sharp as indicated by the increased spacing between the contours (Fig. 3e). This change marked the beginning of a trend of a redistribution of the area of updrafts in the vertical that is reflected in the upward mass transport distribution topography of the CFAD and in the net upward mass transport profiles.

At 2155 UTC, the shape of the downward mass transport distribution topography (Fig. 3g) was similar to what it had been at 2144, except that at altitudes above 5 km the contoured area of less than -50×10^6 kg s^{-1} was broader (roughly extending from -8 to -1 m s^{-1}). At lower levels, net downward mass transport (Fig. 3h) had decreased, while above 5 km, net downward mass transport had slightly increased. The lowering of the level of the strongest upper-level downdrafts (YH Part II, sections 3c,d), compared to previous times, increased the contribution of upper-level downdrafts to net downward mass transport since the decrease in altitude was accompanied by an increase in the density of the air. Thus, the decreasing altitude of upper-level downdrafts was related to the broader contoured area in the downward mass transport distribution topography above 5 km (Fig. 3g) and the corresponding increase in net mass transport above 5 km (Fig. 3h).

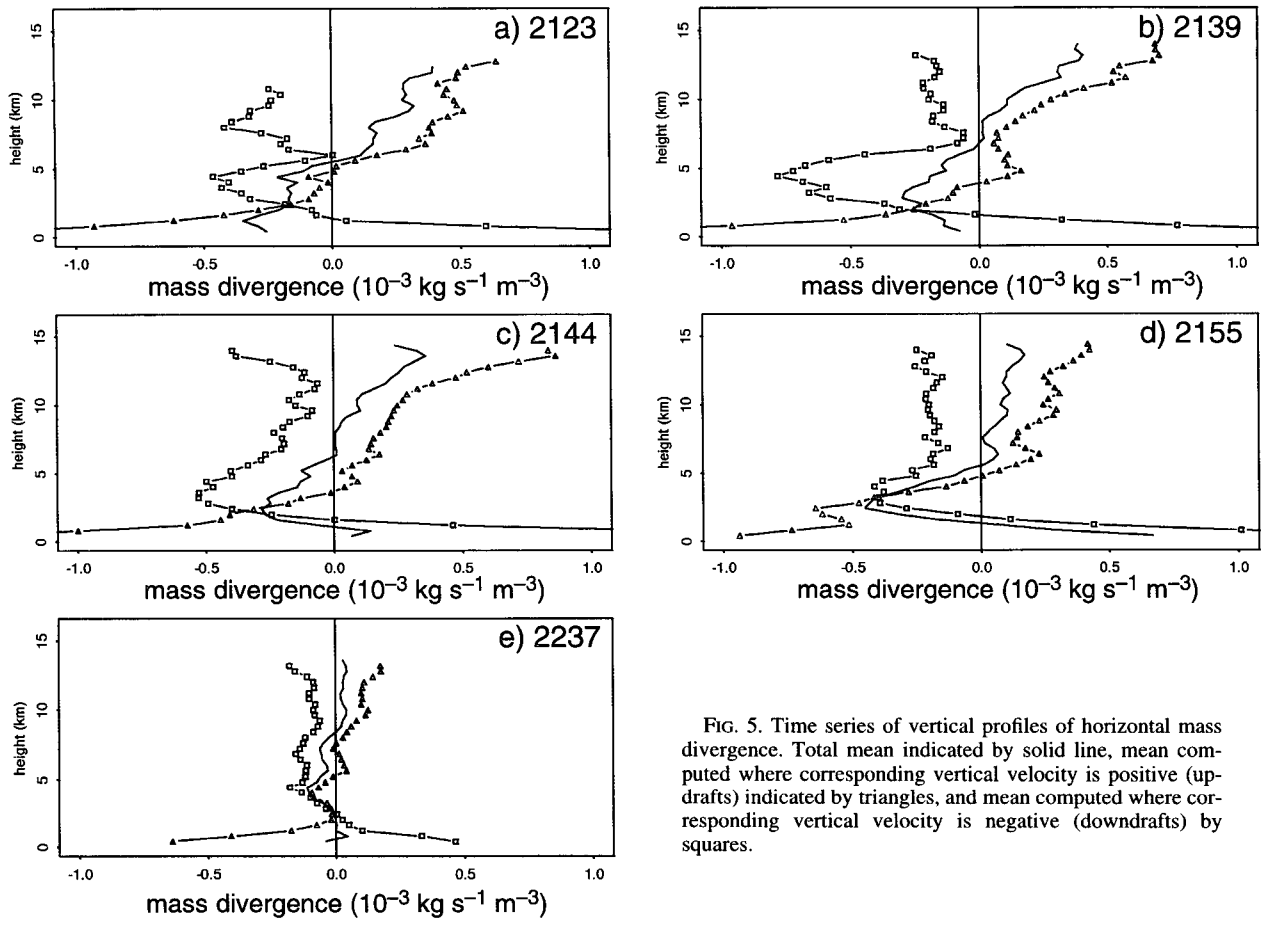

FIG. 5. Time series of vertical profiles of horizontal mass divergence. Total mean indicated by solid line, mean computed where corresponding vertical velocity is positive (updrafts) indicated by triangles, and mean computed where corresponding vertical velocity is negative (downdrafts) by squares.

At 2155 UTC, the peak upward mass transport in the upward mass transport distribution topography shown by the contours in the CFAD was now centered at 5–6 km in altitude and 2–6 m s^{-1} vertical velocity (Fig. 3g). As well as the increased altitude of the center of the peak, there was also a distinct change in the shape of its topography, as indicated by the pattern of contours of the CFADs. The topography of upward mass transport had changed from a high, sharp peak at 2139 UTC (maximum greater than 125×10^6 kg s^{-1} surrounded by closely spaced contours in Fig. 3b), to a shorter, more rounded peak at 2155 UTC (maximum greater than 75×10^6 kg s^{-1} surrounded by widely spaced contours in Fig. 3g). The CFAD changes thus indicate a shift from a high concentration of vertical velocities in a narrow range of intensities at one level to a somewhat broader distribution of intensities and heights.

In the intermediary stage of the storm (2237 UTC), the frequency distribution of vertical velocity had weakened considerably compared to previous times (Fig. 3j of YH Part II). The change in the frequency distribution of downdraft velocity is reflected in the narrow, sharply peaked shape of the downward mass transport distribution topography (Fig. 3i) concentrated near 1 km and -1 m s^{-1}. The predominately weak downdrafts produced a correspondingly weak profile of net downward mass transport (Fig. 3j), which had its maximum value at low levels.

The upward vertical mass transport at 2237 UTC was of a much different character (Fig. 3i), and much reduced (Fig. 3j), in comparison to previous times. The peak in the upward vertical mass transport topography shown by the CFAD was now shaped like a ridge centered near 1 m s^{-1} vertical velocity and extending from near 4 to roughly 10 km in altitude. The narrow range of updraft velocities in the storm (Fig. 3j of YH Part II) is reflected in the narrow distribution of upward mass transport between 1 and 4 m s^{-1}. In order to obtain a ridge in the distribution topography at a roughly constant upward mass transport value ($M_{ij} \sim 75 \times 10^6$ kg s^{-1}) and a constant vertical velocity $w = 1$ m s^{-1}, the area covered by 1 m s^{-1} updrafts must have increased exponentially with height in order to offset the decrease in density with height.

Changes in the topography of the distribution of downward vertical mass transport seen in the CFADs of mass transport in Fig. 3 were primarily related to an

increase in the area of the storm and changes in the frequency distribution of vertical velocity at each level. Overall, a *general characteristic of the downward mass transport distribution topography was that the distribution remained concentrated at low levels throughout the storm evolution.* In contrast, the peak in the upward mass transport distribution topography shifted upward in altitude as the storm matured. Thus, *in addition to changes in storm area and the frequency distribution of vertical velocity at a given height, the evolution of the upward mass transport distribution was related to the changing distribution of upward velocities with height.*

The vertical mass transport in a stratiform echo volume from the 10–11 June 1985 PRE-STORM case (Fig. 4, note change in vertical velocity scale and contour interval from Fig. 3) indicated a continuation of trends seen in the CaPE volumes (see also YH Part II, section 3). The radar echo volume of this storm was much greater than that of the CaPE volumes, so the magnitudes of vertical mass transport are much greater. Similar to the CaPE volumes (Fig. 3), the distribution of downward mass transport in the PRE-STORM stratiform region was concentrated at low altitudes. The CFAD of vertical mass transport in the PRE-STORM stratiform region (Fig. 4a) shows a sharp peak in downward vertical mass transport from downdrafts of near -2 to 0 m s^{-1} centered near 2.5 km. The net profiles (Fig. 4b) show that most of the vertical mass transport for this stratiform region was downward, with the maximum net downward mass transport at 2.5-km altitude. The pattern of contours in the upward vertical mass transport distribution for the PRE-STORM stratiform region (Fig. 4a) exhibited two concentrations of upward vertical mass transport. The stronger peak in the upward mass transport distribution topography was at mid- to upper levels of the storm, produced by upward velocities about 0.5 m s^{-1}, and was centered near 7-km altitude. The location of this peak is consistent with the trend seen at 2155 and 2237 UTC in the CaPE volumes for the peak in the upward mass transport topography to be at midlevels as the storm began to take on stratiform characteristics. Another weaker local maximum in upward mass transport in the PRE-STORM stratiform volume was centered at low levels near 1.5 km and was also a product of upward velocities close to 0.5 m s^{-1} in magnitude. The local maximum in the net upward mass transport curve (Fig. 4b) at 7 km is only slightly stronger than the local maximum at the 1.5-km altitude. The information from both the CFAD of vertical mass transport (Fig. 4a) and the net upward mass transport profile (Fig. 4b) indicates that the area of updrafts near 7 km with $w = 0.5$ m s^{-1} magnitude was more than double that of the area with $w = 0.5$ m s^{-1} at low levels. Thus, similar to the CaPE intermediary volume, there was much more area at midlevels exhibiting weak ascent than at low levels.

3. Horizontal mass divergence associated with vertical motions

The vertical mass transports discussed in section 2 imply associated fields of horizontal mass divergence. The conversation of mass under anelastic conditions is expressed by the continuity equation

$$\nabla_H \cdot \rho_0 \mathbf{V} = -\frac{\partial(\rho_0 w)}{\partial z}, \tag{3}$$

where $\mathbf{V}$ is the horizontal wind vector, ∇_H is the horizontal gradient operator, and ρ_0 is the base-state density (a function of height z only). The horizontal mass divergence ($\nabla_H \cdot \rho_0 \mathbf{V}$) is thus the change of vertical mass flux with height.

As part of the dual-Doppler analysis procedure (YH Part I, section 4), the horizontal divergence is calculated from the Doppler-derived horizontal wind components. The horizontal mass divergence $\nabla_H \cdot \rho_0 \mathbf{V}$ on the left-hand side of (3) is simply determined as the density-weighted horizontal divergence $\rho_0 \nabla_H \cdot \mathbf{V}$, where ρ_0 is the base-state density assumed to be a function of height only.

Mean profiles of the total horizontal mass divergence, the horizontal mass divergence associated with updrafts, and the horizontal mass divergence associated with downdrafts for each of the dual-Doppler volumes have been derived from the Doppler analyses and are presented in Fig. 5. These profiles may be interpreted in light of the vertical velocity, which appears in the term on the right-hand side of (3). By averaging (3) horizontally over the region of radar echo[5] at a given altitude and splitting up the derivative on the right-hand side, we obtain

$$\nabla_H \cdot \rho_0 \bar{\mathbf{V}} = -\rho_0 \frac{\partial \bar{w}}{\partial z} - \bar{w} \frac{\partial \rho_0}{\partial z}, \tag{4}$$

where the overbar represents the horizontal average over the region of echo. The solid curves in Fig. 5 represent the profiles of $\nabla_H \cdot \rho_0 \bar{\mathbf{V}}$ for the entire region of echo, while the curves indicated by triangles and squares represent the profiles of $\nabla_H \cdot \rho_0 \bar{\mathbf{V}}$ for the regions of echo containing upward and downward motion, respectively.

The two terms on the right-hand side of (4) are shown in Fig. 6 for the volume of data taken at 2139 UTC. The curves in Fig. 6a show the two components making up the profile of $\nabla_H \cdot \rho_0 \bar{\mathbf{V}}$ shown by the solid curve in Fig. 5b. The solid curve in Fig. 6a is $-\rho_0 \partial \bar{w}/\partial z$, while the curve indicated by dots is $-\bar{w}\, \partial \rho_0/\partial z$. Similarly, the profiles in Figs. 6b and 6c show the $-\rho_0 \partial \bar{w}/\partial z$ and $-\bar{w} \partial \rho_0/\partial z$ components of the

[5] As in YH Part II, the terms *radar echo region* and *echo region* will be used to indicate the storm volume where radar reflectivity greater than -15 dBZ and vertical velocity could be determined from the dual-Doppler measurements.

updraft and downdraft profiles of $\nabla_H \cdot \rho_0 \bar{\mathbf{V}}$ in Fig. 5b. From the three panels of Fig. 6, it is evident that the term $-\rho_0 \partial \bar{w}/\partial z$ contains most of the structure inherent in the profiles of $\nabla_H \cdot \rho_0 \bar{\mathbf{V}}$ in Fig. 5b. A similar result is obtained for the other times shown in Fig. 5. This result means that we may interpret the horizontal mass divergence profiles in Fig. 5 in terms of the vertical variation of mean vertical velocity $\bar{w}$.

Consider a layer of mean mass divergence ($\nabla_H \cdot \rho_0 \bar{\mathbf{V}} > 0$). In this storm, such a layer of air is populated by rising and or sinking parcels whose dimensions are much less than the region over which the average is taken in (4). Since the first term on the right-hand side of (4) is dominant, net mass divergence in the layer is primarily the result of more parcels slowing and stopping in the layer than speeding up. In contrast, mean mass convergence ($\nabla_H \cdot \rho_0 \bar{\mathbf{V}} < 0$) in a layer indicates that more parcels are accelerating through the layer than slowing and depositing their mass.

In subsequent discussions we will interpret the mean horizontal mass divergence profiles as the net effect of the ensemble of individual parcels accelerating or decelerating as they move through layers of the storm. In examining the changes in the horizontal mass divergence profiles with height in this manner, we will consider how entrainment and gradients of pressure perturbation affect the ensemble of updraft and downdraft parcels moving through the storm.

a. Distribution of divergence

To appreciate the wide distribution of divergence associated with the mean profiles of mass divergence in Fig. 5, CFADs of the total divergence and its updraft and downdraft components for 2139 UTC are shown in Fig. 7. A wide distribution of both divergence and convergence is evident in the updraft and downdraft CFADs. Away from the surface boundary, convergence dominated the average for downdrafts (Figs. 5b and 7b) and divergence dominated the average for updrafts (Figs. 5b and 7c). This pattern suggests that parcels were on average characterized by downward acceleration and upward deceleration, which were probably largely due to entrainment, although pressure perturbation forces associated with the drafts themselves would also have played a role. Mixing with drier environmental air is a positive feedback for the downdrafts, since evaporation cools the air and decreases buoyancy. Following a downdraft parcel, an acceleration of the parcel downward within a layer would increase downward mass transport and be associated with convergence. Divergence occurred as the downdraft air was deposited in the boundary layer, where the air finally had to decelerate. In contrast, entrainment is a negative feedback for updrafts, reducing the positive buoyancy, weakening the updraft as the parcel becomes more diluted with environmental air, and finally bringing it to a stop. Divergence is expected where parcels slow or come to a stop. Thus, divergence would occur

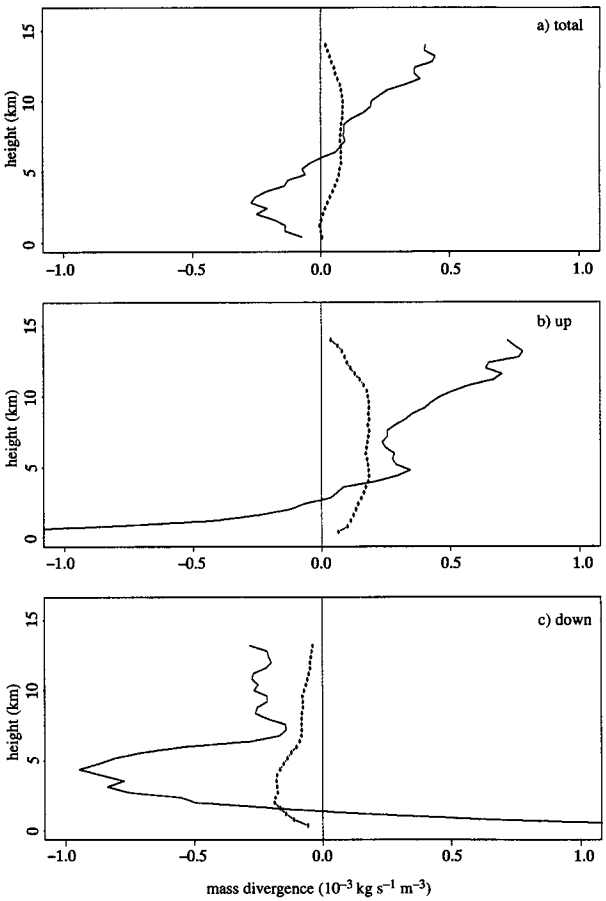

FIG. 6. Comparison of mean horizontal mass divergence terms on right-hand side of Eq. (4) at 2139 UTC. The solid curve is $-\rho_0 \partial \bar{w}/\partial z$, while the curve indicated by dots is $-\bar{w} \partial \rho_0/\partial z$. (a) Total, (b) within updrafts, and (c) within downdrafts. The sum of the two curves in (a) corresponds to the total curve in Fig. 5b. Similarly, the sums of two curves in (b) and in (c) correspond to the updraft and downdraft curves in Fig. 5b.

in layers where updraft parcels tend to become less buoyant as a result of entrainment and, in the case of undiluted parcels, near the level of their maximum height. In both instances mass is being deposited in a layer, and divergence compensates for it.

The wide distribution of values of divergence within updrafts (Fig. 7c) clearly illustrates that while the net effect of the ensemble of updrafts above 4 km yielded divergence and net deposition of mass (Fig. 5b), many individual updraft parcels were in fact accelerating through a given layer and were registered as convergent points in the distribution. The situation is analogous for the wide distribution of divergence values and the mean convergence of the ensemble of downdrafts (Figs. 5b and 7b). Some downdraft parcels deposited their mass within a layer and were associated with divergence even though the mean divergence profile within downdrafts is convergent above 2 km.

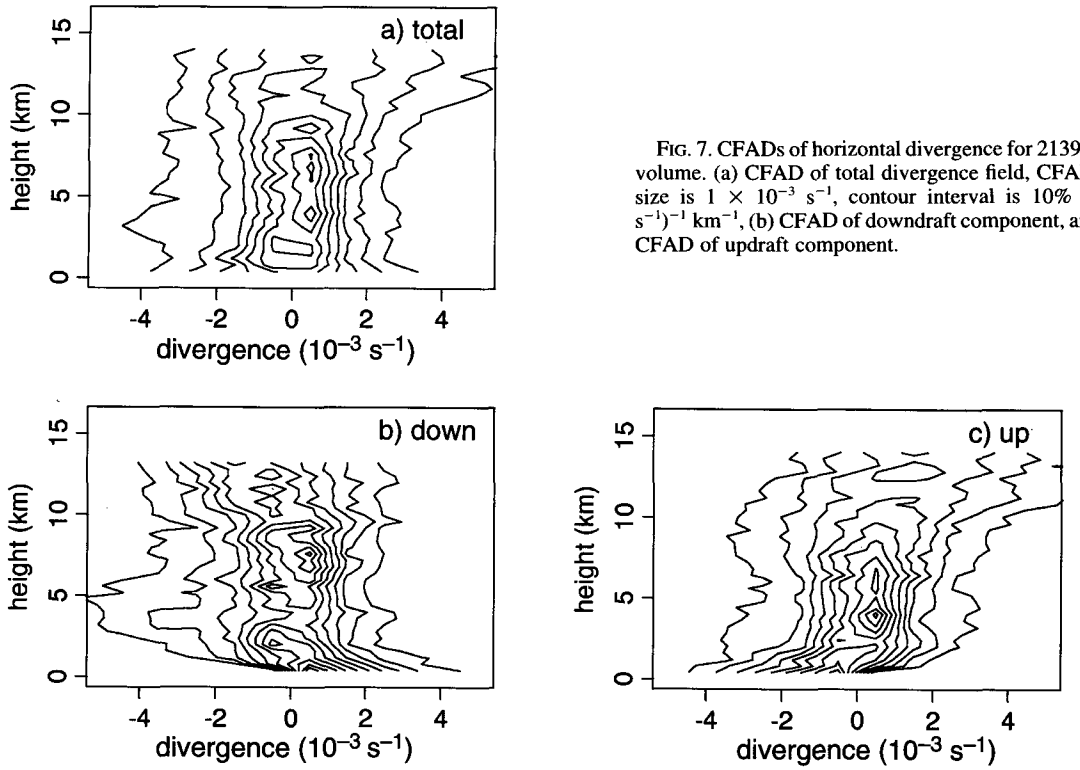

FIG. 7. CFADs of horizontal divergence for 2139 UTC volume. (a) CFAD of total divergence field, CFAD bin size is 1×10^{-3} s^{-1}, contour interval is 10% $(10^{-3}$ $s^{-1})^{-1}$ km^{-1}, (b) CFAD of downdraft component, and (c) CFAD of updraft component.

b. Horizontal mass divergence profiles

The average horizontal mass divergence profiles in the early stages of the storm before the air within the storm became well mixed are represented by Figs. 5a and 5b (2123 and 2139 UTC). The total mass divergence profile at 2139 (Fig. 5b) resembles in shape the typical mass divergence profile for convective regions (Fig. 2c). The maximum of mass convergence is at low levels but elevated off the surface (Mapes and Houze 1993), and mass divergence dominated upper levels.

The peak of mass convergence seen at 4–5 km at all times in Fig. 5 in the downdraft curves reflects the downward acceleration of the downdraft parcels through that layer. This local maximum in mass convergence corresponds to a drier layer in the prestorm sounding (Fig. 3b of YH Part I) and the layer of minimum θ_e, which is identified with initiation of low-level downdrafts (Zipser 1969, 1977; Srivastava 1985, 1987; Knupp 1987). The downdrafts finally weakened as they approached the surface, depositing their mass in the boundary layer and thereby producing a strong divergence signal (downdraft curves in Fig. 5).

The updraft component of the mass divergence profiles in Fig. 5 indicates the behavior of the ensemble of rising parcels. Surface convergence gave them a "kick" upward to rise above the level of free convection. The air associated with the updraft parcels then became increasingly divergent, starting at 4–5 km. This divergent signature at mid- and upper levels is likely due to some of the updraft parcels stopping within those layers and depositing their mass when entrainment eroded their buoyancy. Pressure perturbation forces are also involved in the slowing of rising parcels; these effects are greatest near the updraft top (Ferrier and Houze 1989). For levels starting at 4–5 km, more parcels appear to have been slowing or stopping than accelerating and continuing through. With increasing height, fewer and fewer updraft parcels were available to proceed higher. As the upward-moving parcels slowed and stopped, they deposited their mass, and the overall average was divergent from 4 to 5 km upward.

At levels above 8 km, there is a rough mirroring of the upper-level updraft mass divergence and upper-level downdraft mass convergence (Fig. 5); as updraft divergence increases, so does downdraft convergence. This behavior is a strong argument that the upper-level downdrafts are dynamically forced, that is, that upper-level downdrafts are forced by outflow from upper-level updrafts (YH Part II, section 3d, appendix B). Between 2 and 4 km, the apparent lack of an association between the downdraft convergence and updraft divergence (both are convergent down to the lowest layers) is consistent with the upper- and lower-level downdrafts being physically distinct (Biggerstaff and Houze 1993). The convergence at the top of the lower-level downdrafts is associated with the low-θ_e layer (i.e., dry layer) and the 0°C level. Thus, the lower-level down-

drafts, as expected, appear to be associated with evaporation and melting. Downward vertical mass transport peaked near 2.5 km (Figs. 3b,d,f,h,j), as the downward-moving parcels encountered the surface and spread out in the boundary layer (divergence in the downdrafts below about 2.5 km in Fig. 5). The local minimum in mass convergence near 6–7 km in the downdraft component profiles at 2123 and 2139 UTC (Figs. 5a,b) appears to be the region between the two downdraft regimes where there is no particular mechanism favoring either upper- or lower-level downdrafts.

As the storm matured (Figs. 5c–e), the air within the storm became more well mixed, and correspondingly, the thermodynamic profile (Fig. 3c of YH Part I) became more moist adiabatic. The mixing reduced the differences in thermodynamic properties between adjacent layers. Consequently, at later stages, the air entrained into updrafts and downdrafts from their immediate in-storm surroundings had properties, such as moisture content, that varied more gradually with height than the prestorm environmental air, and the divergence profiles exhibited smaller variations between adjacent layers.

The total mass divergence profile at 2237 UTC (Fig. 5e) resembles the shape of the typical mass divergence profile for stratiform regions (Fig. 2c). As noted in YH Part I, the storm did not yet display a fully stratiform structure in spatial cross sections, but it displayed a narrowing reflectivity distribution (Fig. 3i of YH Part II) that indicated it was in transition from convective to stratiform structure. The profile for this time is divergent near the surface, has maximum convergence near the 0°C level, and is weakly divergent aloft. The peak mass convergence in the profile at 2237 UTC (Fig. 5e) had moved upward to the 4.5-km altitude from 3 km at 2155 UTC (Fig. 5d). This peak in mass convergence is associated with the downward vertical transport distribution at 2237 UTC (Fig. 3i), which shows a sharp increase in downward mass transport below 5 km contributed by -2 to -1 m s^{-1} downdrafts. The layer of low-θ_e air was less distinct and had moved downward during the development of the storm (Fig. 3b,c of YH Part I). It is possible that whereas in the early stages of the storm the effects of the dry low-θ_e layer had a strong influence on the acceleration of downdrafts downward, in later stages, when the air was more moist, the effects related to the change of phase of falling precipitation particles dominated and the increase in acceleration of downdrafts occurred closer to the 0°C level (Leary and Houze 1979).

The mass divergence profiles elaborate on the conclusion from the vertical mass transport distributions (section 2) that most of the mass transport was occurring at low levels. Mass divergence predominated in updrafts above the 4–5-km altitudes to storm top. Thus, it appears that from the initial wide distribution of positively buoyant parcels at the low levels in the storm, only the most buoyant and most undiluted parcels made it to the top; the rest deposited their mass throughout the depth of the storm at whatever level their upward motion was stopped. The generally decreasing mass convergence and then increasing mass divergence associated with the ensemble updrafts above the boundary layer is consistent with Raymond and Blyth's (1986) conclusion that environmental air is mixed into the cloud at all levels and thus may be entrained anywhere along a parcel's trajectory. Hence, the upward progress of the parcel may be halted at any level.

4. Vertical mass transport during the convective-to-stratiform transition

A major goal of this study is to determine how a storm arrives at the typical mean vertical velocity profile in stratiform regions (Fig. 2b) of weak mean descent of air below the 0°C level and weak mean ascent above. It is well established that downward-moving air associated with precipitation at low levels accounts for the weak downdrafts below the 0°C level seen in mean vertical velocity profiles in stratiform precipitation (Zipser 1977). While downdrafts dominate the mean vertical velocity profile at low levels, the lower levels of the storm in stratiform regions do not exclusively contain downdrafts. The CFADs of vertical velocity and vertical mass transport have illustrated that weak updrafts are present at low levels in the stratiform stages of a storm. The signature of the low-level weak updrafts is washed out in the mean profile by the increasingly numerous weak downdrafts at low levels (Figs. 4 and 6 in YH Part II).

The origin of the weak updrafts above the 0°C level in stratiform regions is more difficult to explain. Prior studies (Gamache and Houze 1982, 1985; Houze and Rappaport 1984; Smull and Houze 1987; Biggerstaff and Houze 1991, 1993) have established the existence of convergence at midlevels in stratiform regions (Fig. 2c) and mean upward motion in mid- to upper levels. However, because previous studies did not have information available that revealed the sequence of events that occurred as the storm underwent the transition from convective to stratiform stages, considerable ambiguity has remained regarding what these events are and how they interrelate. As discussed in previous sections, the CFADs of the ensemble properties of an entire storm have permitted us to see progressive changes in the ensemble properties as the storm evolved. The information about the progressive changes in the storm ensemble properties will be used in this section as the basis for a hypothesis for how the convective-to-stratiform transition occurs and, in particular, to explain the origin of the weak mean upward motion above the 0°C level in stratiform regions.

To diagnose the primary mechanism of convective-to-stratiform transition, we need to find a descriptor that changes as the storm evolves, and changes in a manner that is clearly consistent with all the other observed changes that occur in the storm during the transition. The vertical-mass-transport-weighted CFADs of ver-

tical velocity (Fig. 3) show clearly that the topography of the distribution of upward vertical mass transport changed progressively from being concentrated at low levels to being concentrated at midlevels. In contrast, the topography of the distribution of downward mass transport remained centered at low levels throughout the development of the storm. Also, the vertical-mass-transport-weighted CFADs of vertical velocity showed that the majority of the mass transport in each volume was accomplished by the moderate (middle income) vertical velocities and that changes in the magnitudes of the few strongest vertical velocities within the volume had a relatively small effect on the net vertical mass transport. *Thus, the most substantial change was in the vertical distribution of the upward velocities of moderate strength, indicating that these upward velocities were the primary agents in the convective-to-stratiform transition.* In this section, we will focus on the changing vertical distribution of moderate strength upward velocities and what it implies physically in the storm regarding how the convective-to-stratiform transition takes place.

The evolution of the distribution of moderate-strength upward velocities with height provides insight into the evolution of the kinematics of the storm from convective to stratiform stages. Figure 8 shows the number of points at each level, which is proportional to area covered, with velocities between 1 and 5 m s^{-1}, the range of velocities indicated as having the most effect on the evolution of the storm. During the highly convective stages of the storm (2123, 2139, and 2144 UTC), the majority of parcels with vertical velocity 1 m $s^{-1} < w < 5$ m s^{-1} were at low levels (Fig. 9). At later stages of the storm (2155 and 2237 UTC), the maximum area of updraft parcels where 1 m $s^{-1} < w < 5$ m s^{-1} is centered at 9–10-km altitude (Fig. 8).

To show more clearly how the upward mass transport changed in character as the storm evolved, the location in w-height space of the center of the peak of upward-mass-transport distribution topography seen in the CFADs of Fig. 3 is shown for each of the five volumes in Fig. 9a. In addition, the 50×10^6 kg s^{-1} upward vertical mass transport contours for 2123, 2155, and 2237 UTC from Fig. 3 are superimposed in Fig. 9b. In Fig. 9a, the movement of the center of the peak in upward-mass-transport distribution topography horizontally represents changes in the frequency distribution of vertical velocity at a level, and the movement of the center of the peak in upward mass transport distribution topography vertically represents changes in the distribution of vertical velocity with height.

In its early stages (2123 and 2139 UTC), the storm was generally convective and had only barely begun the transition from convective to stratiform. The profile of mean vertical velocity at 2139 (Fig. 6b of YH Part II) was similar to a typical profile of vertical velocity in convection (Fig. 2b). Vertical mass transport greater than 50×10^6 kg s^{-1} at 2123 was all below 6 km and

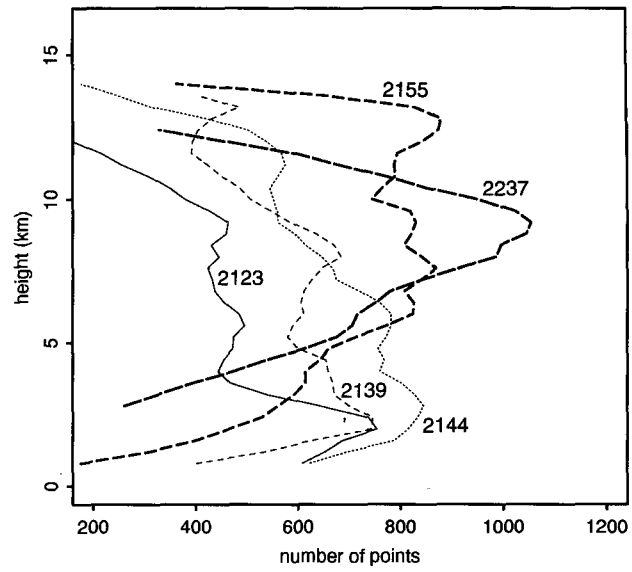

FIG. 8. Vertical profiles of number of points at each level (proportional to area) with vertical velocities between 1 and 5 m s^{-1} for the five dual-Doppler volumes.

had contributions from a range of updrafts up to 9 m s^{-1} (Fig. 9b). Peak vertical mass transport values at 2123 were being accomplished by upward velocities of approximately 1 m s^{-1} at the 1-km altitude (Fig. 9a). As the storm became more vigorous (2139 UTC), the peak in the distribution of vertical mass transport topography remained essentially stationary between 2123 and 2139 UTC. At 2144, the storm was at its most vigorous stage and the peak in the distribution of vertical mass transport topography had moved to the right, reflecting the widening of the distribution of upward velocities at low levels (Fig. 3f of YH Part II). In addition, the peak in the distribution of vertical mass transport topography at 2144 had moved upward to 2.5 km, reflecting the beginning of a change in the vertical distribution of updrafts. As the storm began to weaken (2155 UTC), the peak in the distribution of vertical mass transport topography split into two centers. The centroid of the two peaks had moved to the left, corresponding to the narrowing of the distribution of updrafts below 5 km (Fig. 3h of YH Part II), and further upward, corresponding to a change in the relative distribution of upward mass transport with height. Vertical mass transport exceeding 50×10^6 kg s^{-1} at 2155 had also shifted upward but remained broad, encompassing vertical velocity values from 1 to over 9 m s^{-1} (Fig. 9b). At 2237, characterized as intermediary between convective and stratiform by its vertical velocity profile (Fig. 6e of YH Part II), the peak in the distribution of vertical mass transport topography was a ridge with two local maxima. The centroid of the ridge's peak had moved further to the left, corresponding to the further narrowing of the distribution of updrafts toward 0 m s^{-1} (Fig. 3j of YH Part II). The shape of the area

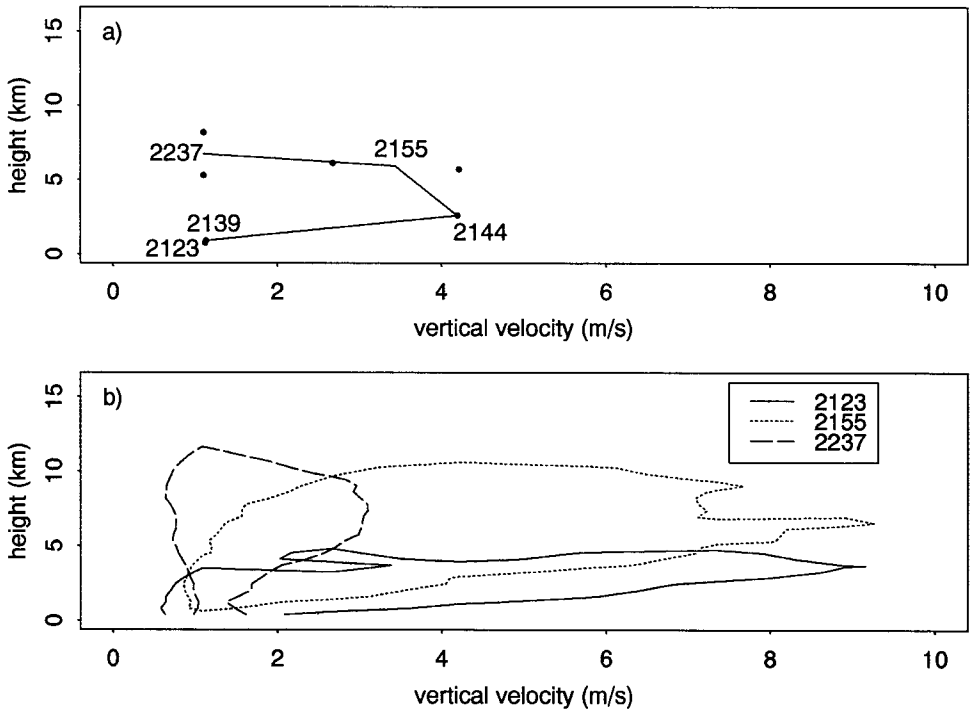

FIG. 9. Evolution of upward mass transport. (a) Approximate location of centroid of peak in upward mass transport for 2123, 2139, 2144, 2155, and 2237 UTC volumes connected by line segments. Dots are positions of local maxima at each time. (b) Contours of upward vertical mass transport equal to 50×10^6 kg s^{-1} at 2123, 2155, and 2237 UTC from CFAD of vertical mass transport (Fig. 3).

outlined by the 50×10^6 kg s^{-1} contour had narrowed to include only vertical velocity values less than 3 m s^{-1} (Fig. 9b).

Thus, in the early stages of the storm (2123 and 2139 UTC), most of the updraft area and upward mass transport were at low levels. Updraft area and upward mass transport then began to shift upward (beginning at 2144 UTC). At later stages of the storm life cycle (2155 and 2237 UTC), most of the updraft area and upward mass transport were at mid- and upper levels of the storm. As the storm evolved, the area of the storm occupied by weak upward vertical velocity at upper levels was growing in horizontal scale at the same time that the intensity of the updrafts was decreasing at these levels. This behavior of the updrafts can be explained if the updrafts are thought of in terms of parcels that behave like buoyant, rising bubbles,[6] a hypothesis advocated by Scorer and Ludlam (1953) and supported by high-spatial-resolution observations and modeling (Raymond and Blyth 1986, 1989). The interpretation of the updrafts as bubbles is also consistent with impressions obtained from the vertical cross sections (described in YH Part I, Sec. 5b).

New updraft parcels are added from the bottom of the storm. If the populations of parcels behaved like populations of buoyant bubbles, they would detach from the surface, move upward, expand, and continue to rise until they reached a stability boundary like the tropopause or their buoyancy was eroded by entrainment so that they could not rise any further. The weaker updraft parcels at upper levels were likely moderate to strong updraft parcels near the surface. Parcels that started near the surface as weak updrafts were weakly buoyant to begin with; their buoyancy would likely be eroded completely before they could reach upper levels.

Upward mass transport increased at upper levels but decreased at lower levels as the storm evolved (Fig. 9b). The distribution of updraft vertical velocity at low levels (Fig. 3 of YH Part II) is assumed to be related to the distribution of updraft parcel initial buoyancy. In the early stages of the storm, a wide distribution of updraft strengths was associated with populations of bubbles with a wide range of buoyancies. These were created and began their ascent, the more buoyant parcels on average rising to higher altitudes than their weakly buoyant cousins. The narrowing of the distribution of vertical velocity indicates that as the storm evolved there were a relatively greater number of less buoyant parcels and a relatively smaller number of more buoyant parcels produced. Overall, upward mass

[6] Our use of the term bubble denotes a positively buoyant element without a "skin" but otherwise exhibiting bubble-like behavior.

transport at low levels decreased. Upward mass transport at mid- and upper levels increased as parcels congregated at those levels. Even though the parcels at mid- and upper levels were primarily weak (Fig. 3 of YH Part II), so many updraft parcels had congregated (as indicated by the relative increase in area of updrafts in Fig. 8) that despite the density weighting of mass transport, these updraft parcels at mid- and upper levels collectively became the important movers of air mass upward in the later stages of the storm.

The vertical mass transport distributions (Fig. 3) along with the CFADs of vertical velocity (Fig. 3 of YH Part II) indicate the following evolution for the kinematics of the storm. Starting with a quiescent state ($w = 0$), a distribution of weak and strong updraft parcels associated with boundary layer convergence were introduced in localized areas and moved upward. Downdrafts associated with both the buoyancy perturbation of the updrafts and with precipitation were produced. As bubbles of positively buoyant air rose (with and without entrainment) toward their maximum heights, they flattened, encompassing more area and weakening overall. As the storm matured, what started as a few locally concentrated updrafts within a small area of an otherwise quiescent fluid evolved into weak motion over wide areas within the storm. Thus, updraft parcels appeared to rise from low levels and congregate at upper levels as they slowly weakened and spread out. *It is hypothesized on the basis of these results that populations of weakened spreading updraft parcels account for the mean upward motion above the 0°C level seen in mean vertical velocity profiles in stratiform precipitation (Fig. 2b).*

5. Particle fountain conceptual model

The ensemble properties derived from the high spatial resolution of the radar measurements in this study have provided useful constraints on the interpretation of processes occurring in the storm. The CFADs of vertical velocity, vertical mass transport, and horizontal mass divergence define the kinematic behavior of the ensemble of updrafts and downdrafts within the storm and thus place constraints on interpretations of the behavior of individual updraft and downdraft parcels. We have postulated behavior of individual updraft parcels that fits within the pattern evident from the ensemble properties (sections 3 and 4). The vertical-mass-transport-weighted CFADs of vertical velocity further indicate the environments within which the storm's microphysical processes occurred, while the CFADs of reflectivity and differential reflectivity indicate the ensemble characteristics of those microphysical processes (section 5, YH Part II). In this section, the statistical constraints comprised by the CFADs on the behavior of all facets of the storm (both kinematic and microphysical) will be combined and interpreted in terms of a conceptual model.

The behavior of buoyant parcels observed in this study is consistent with the conceptual model described by Raymond and Blyth (1986) derived from in situ aircraft observations and modeling and subsequently extended using ground-based radar observations (Raymond and Blyth 1989; Raymond et al. 1991). In their conceptual model (illustrated schematically in Fig. 10), parcels have a range of initial buoyancies and experience various amounts of entrainment during their ascent. Only the "lucky," initially strongly buoyant, undiluted parcels reach cloud top. Most parcels are slowed and stopped along the way. These ideas are an outgrowth of bubble-based or thermal convection conceptual models derived from observational and modeling studies over the past 40 years (Ludlam 1952; Scorer and Ludlam 1953; Warner and Telford 1963; Fritsch 1975; Browning et al. 1976; Dye et al. 1983 and others). The vertical-mass-transport-weighted CFADs of vertical velocity in Fig. 3 add to Raymond and Blyth's conceptual model by showing the relative contributions of different strength drafts to the vertical mass transport within the entire storm. The distribution of vertical velocities at different levels (Fig. 3 of YH Part II) and the mass divergence profiles (Fig. 5) confirm that updraft parcels are slowing and stopping at all levels within the storm. The vertical mass transport distributions in Fig. 3 also show a systematic rearrangement of upward-moving air in the storm that starts concentrated at low levels and becomes concentrated at midlevels (Fig. 9b). This phenomenon can be explained in terms of positively buoyant elements or bubbles, originating at the surface in large numbers at the initial stages of the storm, slowing, stopping, and congregating at mid- and upper levels as the storm matures. At the same time production of more buoyant elements at low levels decreases (section 4).

Closely interrelated to the dynamics of the storm described above was the microphysical evolution of the storm. The microphysical evolution was characterized by the majority of the volume of the storm containing falling particles—consistent with the predominately weak vertical velocities within the storm that are insufficient to suspend the snow particles that were shown by CFADs of differential reflectivity to have been present throughout the mid- and upper levels of the storm (Fig. 10, YH Part II, section 4).

A conceptual model aimed at explaining the microphysical structure of cumulonimbus was advanced by Hobbs and Rangno (1985) (Fig. 11) and extended in Rangno and Hobbs (1991). It was based on in situ aircraft observations of cumuliform and stratiform clouds in a midlatitude maritime regime. This conceptual model describes well the basic microphysical characteristics of the storm observed on 15 August 1991 in Florida. The stronger updrafts injected ice particles into mid- and upper levels of the storm, heavier particles fell out faster (within ice strands associated with collapse of updraft in Fig. 11), and lighter particles were spread with the prevailing upper-level wind into the anvil where they eventually fall out (aggregation zone and precipitation in Fig. 11). The high-resolution

three-dimensional volumes of Doppler and polarimetric radar data employed in this study provide additional information about these microphysical processes by indicating the distribution and types of precipitation-sized hydrometeors at different altitudes in the storm and how those distributions changed as the vertical velocity distribution in the storm evolved (Figs. 3 and 10 of YH Part II). Also, by looking at the entire storm, as we are able to do with the CFADs, the effects of the strongest updrafts can be put in context.

We will combine the basic tenets of the Raymond and Blyth (1986) conceptual model regarding the dynamic behavior of buoyant air parcels and Hobbs and Rangno's (1985) conceptual model regarding the behavior of ice particles within the storm. The resulting conceptual model will then be used to describe the convective-to-stratiform transition of the storm.

The basic building block of this fused conceptual model is called a particle fountain.[7] It consists of an updraft behaving like a buoyant bubble and its accompanying precipitation particles and pressure gradient–forced downdrafts. Various aspects of particle fountains are illustrated in Figs. 12–15. The particle fountain distributes liquid water and ice particles into the mid- and upper levels of the storm in a manner resembling a fountain spurting water drops (Fig. 14c). This unit of convection initially has a horizontal scale of 1–3 km. Its upper portion corresponds to a convective turret as defined by Hobbs and Rangno (1985) (Fig. 11). As an extension to the concept of a buoyant "bubble," a particle fountain serves to describe how the vertical redistribution of upward-moving air, an integral part of the convective-to-stratiform transition of the storm (section 4), is accomplished. Additionally, particle fountains describe the concurrent microphysical evolution of the storm from convective to stratiform stages, that is, an initial wide distribution of reflectivity aloft evolving into a nearly homogeneous reflectivity at each level and an increasing reflectivity with decreasing height (Fig. 3 of YH Part II).

For simplicity, we will approximate the weak vertical wind shear environment of the 15 August 1991 storm by imagining that no vertical wind shear is present. Work is proceeding (M.-J. Yang 1994, personal communication) to address the behavior of particle fountains in various conditions of vertical wind shear. In keeping with our simplification of no vertical wind shear, the updraft parcels that constitute the particle fountains are shown as rising straight up. In reality (i.e., in the presence of environmental shear), updraft parcels have sloping three-dimensional trajectories (Fig. 11).

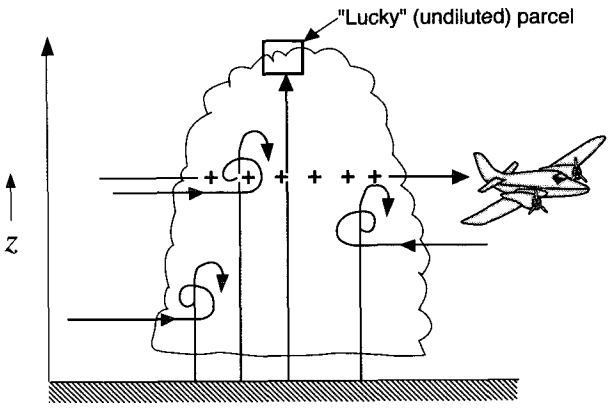

FIG. 10. Conceptual model of the environment of a cumulus cloud in which air parcels rising from cloud base to aircraft flight level have mixed in various fractions with air entrained near flight level. Parcels entrain air at a variety of levels and come to rest as they lose their positive buoyancy. Cloud top is determined by the maximum height achieved by the "lucky" parcels, which suffer no entrainment and may rise undiluted to their level of zero buoyancy. Adapted from Raymond and Blyth (1986).

Lower-level downdrafts associated with precipitation are interspersed throughout the storm during its evolution (Fig. 3, YH Part II). The mechanisms behind precipitation-associated downdrafts are fairly well understood (Zipser 1969, 1977; Srivastava 1985, 1987; Knupp 1987, 1988). Precipitation-associated downdrafts were present but are not drawn in Figs. 12–15 in order to simplify the diagrams and focus attention on the new insights into the convective-to-stratiform transition presented in this study. We noted in section 2b(2) that the downdraft mass transports remain at the same levels in the lower troposphere throughout the storm's lifetime, while the updraft mass transports evolve. Thus, focusing on the updrafts should lead to insights into the changeover from convective to stratiform structure.

The particle fountain is hypothesized to be a few kilometers in horizontal scale and to have a vertical scale related to the maximum height reached by the updraft parcels that comprise it. The maximum height of the particle fountain is related to initial buoyancy, size, amount of entrainment, and pressure perturbation forces. Figure 12 shows a simplified version of the conceptual model for positively buoyant elements of the same initial buoyancy and size but with different entrainment rates. The buoyant bubbles broaden with increasing height as their volume increases as a result of entrainment and in inverse proportion to pressure. As the parcels comprising the particle fountains slow and stop as they reach their maximum height, they deposit their mass of air and laterally spread the load of hydrometeors they are carrying. A set of particle fountains of different vertical extents thus spreads hydrometeors

[7] Rangno and Hobbs (1991) and Fulton and Heymsfield (1991) used the term "fountain" in a similar way. The analogy between water fountains and the lifting, spreading, and falling of ice particles within particle fountains is one of general appearance and is not to be taken literally in the physical sense. A water fountain works primarily by gravity. Depending on the design of the nozzle configuration, water drops may have a horizontal component to their motion and thus may move laterally as they rise and fall. In particle fountains, a combination of gravity, the expansion of parcels, and friction controls the trajectory of individual particles.

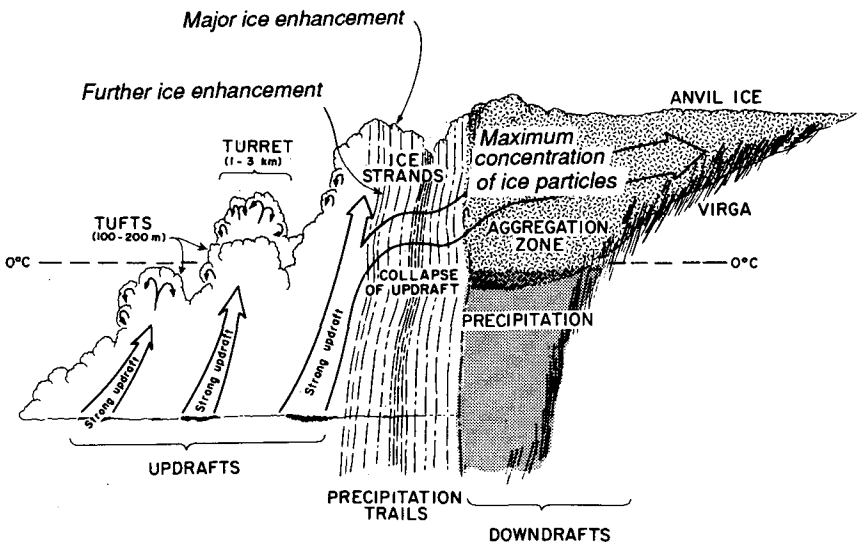

FIG. 11. Empirical model of a small cumulonimbus cloud based on 90 research aircraft penetrations of small cumulonimbus and large cumulus clouds. Adapted from Hobbs and Rangno (1985).

at a variety of levels within the storm. Since strongly buoyant, undiluted parcels are relatively rare, most of the particle fountains do not extend to the top of the storm.

Associated with the buoyancy of the rising parcels are pressure-gradient accelerations required to move the environmental air around to maintain mass continuity (Fig. B1, YH Part II). These forces (indicated by the open arrows in Figs. 12a,b) produce the strong upper-level downdrafts, which in the CFADs (Fig. 3, YH Part II) are consistently associated with the updrafts in time and height (YH Part II, sections 3c,d) and in vertical cross section (Figs. 7b, 9b–d of YH Part I, section 5) are typically adjacent to the updrafts.

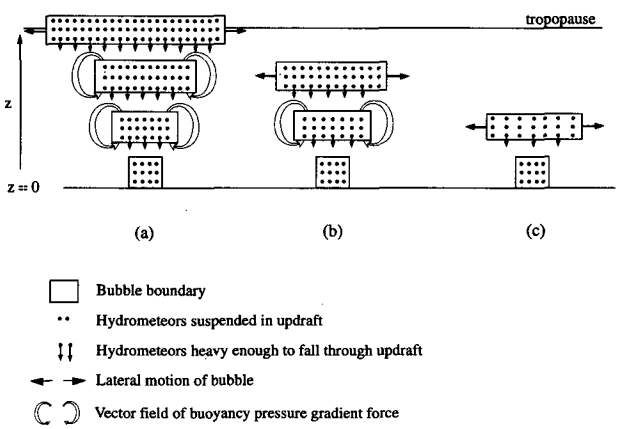

FIG. 12. Conceptual model of an updraft behaving like a buoyant bubble with different entrainment rates. (a) Undiluted, (b) moderately entraining, (c) heavily entraining. Dots indicate hydrometeors suspended by updraft; downward-pointing arrows indicate particles heavy enough to fall through updraft; horizontal arrows indicate lateral spreading of bubble. Open arrows represent the vector field of the buoyancy pressure gradient force as adapted from YH Part II, Fig. B1.

When undiluted bubbles (Fig. 12a) reach the tropopause, they flatten (Lilly 1988) (Fig. 13). The more diluted bubbles (Figs. 12b,c) lose their buoyancy and stop before they reach the tropopause. Those bubbles experiencing less entrainment (Fig. 12b) have their buoyancy eroded more slowly and become nearly neutrally buoyant at higher levels in the storm than their more diluted colleagues (Fig. 12c). When the bubbles reach their level of neutral buoyancy, they slow and spread horizontally (Scorer and Ludlam 1953). When a buoyant parcel slows and stops rising by becoming neutrally buoyant by either dilution or by encountering a stable layer, it deposits its mass of air in that layer and is associated with divergence. Pressure perturbations associated with the rising parcel provide a downward pressure gradient force within the buoyant element (YH Part II, appendix B). This force acts against buoyancy and assures that the divergent layer is of finite rather than infinitesimal thickness. This kinematic behavior of the cloud has an important implication for the storm precipitation structure. The divergence of parcels acts to laterally spread the load of particles transported upward by the parcel (Figs. 12 and 13).

All of the rising parcels carry a load of hydrometeors consisting of liquid water and/or ice particles, the latter created by some combination of ice nucleation, ice enhancement, vapor deposition, freezing, and riming within the updraft. In the 15 August 1991 storm, there was generally not enough time (<30 min) for small ice particles to grow to precipitation size by vapor deposition. The ice particles must then have reached precipitation size by aggregation and/or riming (Hough-

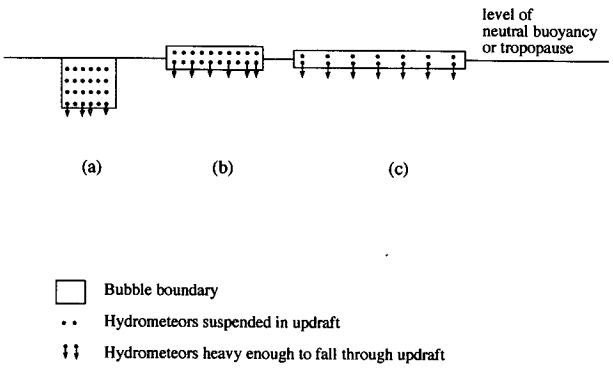

FIG. 13. Conceptual model of a positively buoyant element reaching tropopause and spreading laterally. (a) Buoyant element just reaches tropopause, (b) buoyant element spreads out laterally and thins while at the same time buoyancy is diluted, (c) buoyant element has spread out and weakened to the point where the smaller particles previously suspended can now fall out. As the buoyancy of the bubble is slowly eroded, first the heavier and then the lighter particles previously suspended fall out. Symbols are the same as in Fig. 12. Adapted from Lilly (1988).

ton 1968). Indeed, the differential reflectivity CFADs (YH Part II, section 4) indicated the predominance of aggregates and the presence of some graupel. The heavier particles fall out within the updrafts (Fig. 14b), while the lighter ones, primarily ice particles and possibly small drops, are spread out laterally when the updraft parcel slows (Fig. 14a). This process is consistent with Hobbs and Rangno's (1985) observations that the heavier ice particles fall through the decaying updrafts and may appear as striations in the precipitation below cloud base, while the smaller ice particles are carried laterally outward and upward into the developing anvil portion of the cloud. The ensemble of trajectories for heavier and lighter particles associated with the group of updraft parcels comprise the particle fountain (Fig. 14c).

Updraft parcels stopping at warmer levels might contain hydrometeor mass in the form of liquid water droplets. Updraft parcels that reach higher levels contain progressively more ice. The particles that fall out of the updraft parcels continue their fall through the environment of predominantly weak vertical velocity that dominates the region between the few strong updrafts and downdrafts (Figs. 3 and 4, YH Part II). The upper-level downdrafts adjacent to the rising bubble may evaporate some particles as the relative humidity of unsaturated air is decreased by subsidence (Biggerstaff and Houze 1993); however, the residence time of particles in these downdrafts is probably short (Braun and Houze 1994). The vast majority of particles are in an environment of near zero vertical velocity (Fig. 3, YH Part II), fall slowly, and may increase in size. The ice particles are spread laterally away from the center of the updrafts by the diverging updraft parcels. The slowly falling ice particles between strong updrafts readily explains the filling in of reflectivity between cells as a storm develops (Figs. 8a and 8b of YH Part I, section 5). A few strong particle fountains spreading ice particles at upper levels would likely be sufficient to distribute enough smaller ice particles into the upper levels of the storm to fill in the weaker vertical velocity space between the strong updrafts with small ice particles. Thus, the areas of highest reflectivity associated with the stronger updrafts become connected by regions filled with lower reflectivity ice particles, and the storm appears more continuous in cross section. The filling in of reflectivity between updrafts at mid- and upper levels by particle fountains is consistent with observations of Westcott (1994) and augments the process of merging of individual cumulus clouds initiated at low levels as described by Simpson et al. (1980).

An idealized collection of particle fountains in a multicellular storm is shown conceptually in Fig. 15. The vertical mass transport plots (section 2, Fig. 3) indicate that it was the more numerous moderate-strength vertical velocities that carried most of the burden of moving the air upward in the storm. Figure 15 illustrates a complex situation with particle fountains of different strengths and vertical extents acting in concert to fill the area between them with ice particles. The distribution of the vertical extents of individual particle fountains at any one time means that particles are deposited throughout the depth of the storm. The precip-

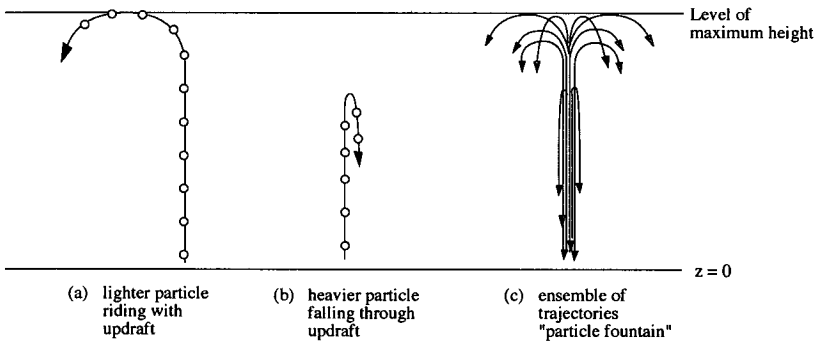

FIG. 14. Conceptual model of hydrometeor trajectories within a particle fountain. (a) A single lighter particle, (b) a single heavier particle, and (c) ensemble of trajectories in a particle fountain.

itation particles deposited at midlevels have less distance to fall and less time to grow than those that begin to fall at higher levels. Many of the updraft parcels, and thus the particle fountains in which they were organized, do not reach storm top and thus cannot deposit their particle load at storm top. Some of the updraft parcels and their associated particle fountains reach the tropopause and spread their particles at the highest levels of the storm. Some of the ice particles deposited near the tropopause are too small to fall, and cirrus clouds develop and extend as anvil from the upper levels of the storm (e.g., Fig. 4, YH Part I).

The few strong updrafts within the storm, although not responsible for much overall mass transport, play an important role by injecting ice particles at upper levels of the storm. The injected ice is spread laterally, and the precipitation-sized ice drifts downward in the environment of weak vertical velocity comprised of the slightly buoyant parcels that slowed and spread laterally at lower levels. This environment of weak ascent is favorable for growth by deposition and aggregation (Rutledge and Houze 1987; Braun and Houze 1994). Once ice is introduced by the early particle fountains, it aids in the rapid glaciation of supercooled raindrops (YH Part II, section 5b) and begins the trend toward stratiform microphysical characteristics seen in the diagonalization of the frequency distribution of reflectivity seen in the reflectivity CFADs (Fig. 3, YH Part II).

Since most of the storm's upward mass transport and hence condensation occurs in regions of weak ascent, particles are dispersed into these regions by particle fountains, and this environment is favorable for particle growth. It follows that most of the mass of precipitation particles is attained in these regions. Thus, the regions between intense updrafts—far from being zones of inactive debris—are regions of significant precipitation growth. In effect, the intense updrafts whose parcels reach upper-tropospheric levels before slowing and spreading provide seed particles for the growth regions, which are located between the intense updrafts.

The evolution of a storm from convective to stratiform stages (section 4) can be related to the conceptual model of the particle fountain as follows. Individual particle fountains complete their life cycle on a timescale less than that of the overall storm. A few are created in the early stages, most are born in the most vigorous stages of the storm, and fewer are created as the storm weakens. As the storm matures past its most vigorous stage, more particle fountains are in their later stages than in their earlier stages. In their later stages,

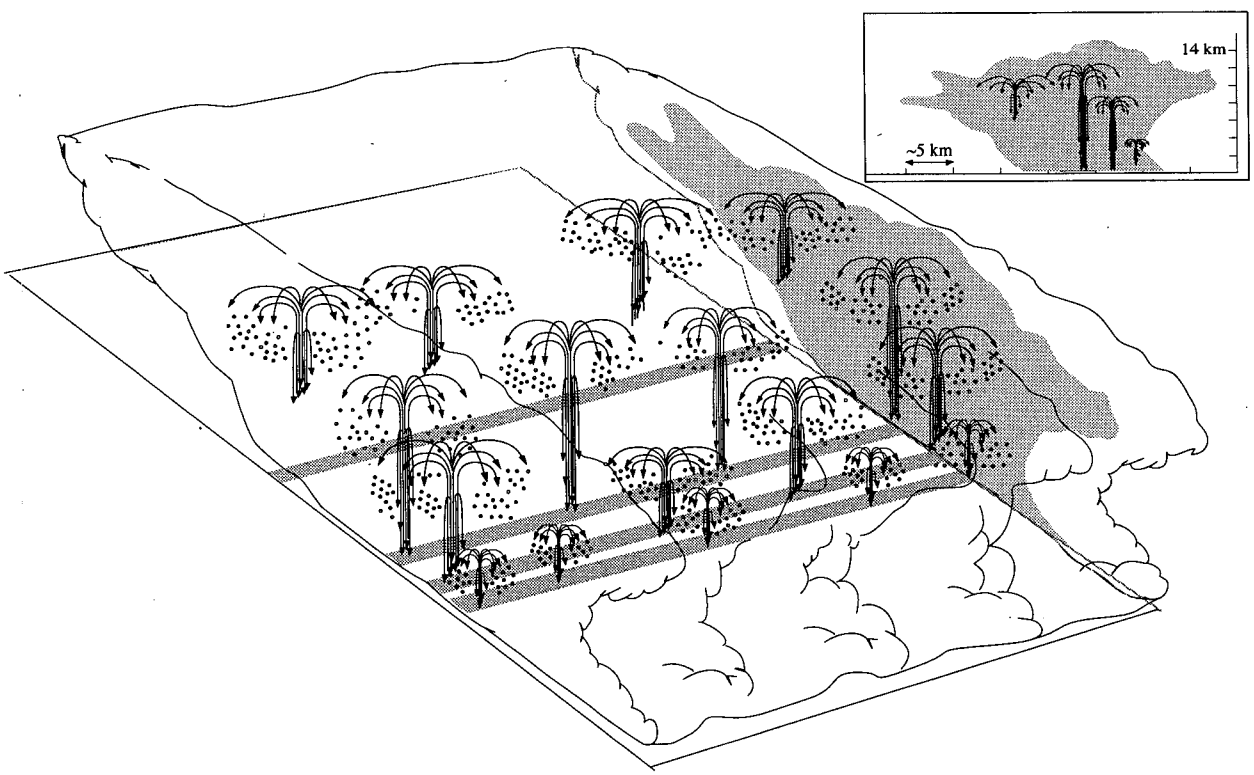

FIG. 15. Conceptual model of an ensemble of particle fountains in a multicellular storm in perspective view. Shaded area represents radar reflectivity echo along a cross section perpendicular to the line of storms. Cloud boundary indicated by scalloped outline. Inset shows approximate scales and arrangement of largest particle fountains relative to radar echo.

particle fountains are nearly neutrally buoyant bubbles of air that slowly spread and weaken. It is these remnants of the updrafts still present at mid- and upper levels that create the upward vertical velocity and average weak divergence in stratiform region mean vertical velocity and mass divergence profiles (Figs. 2b,c). The slowly rising and spreading parcel remnants, which comprise the later stages of a particle fountain, form an ideal environment within which the falling particles can grow as they settle out.

The apparent lag between the kinematic and the microphysical evolution of the storm, such that the ensemble properties of the radar reflectivity begin to take on stratiform-like microphysical characteristics while kinematically speaking the storm is still in its convective stage (YH Part I, section 3), can be understood in terms of particle fountains. In the early stages of a storm, a few young particle fountains are spewing out particles. In the highly energetic and most vigorous stages, more particle fountains are present, and they have a wider range of ages. The particles that they laterally distribute fall out through an environment dominated by weak vertical velocity. By the dissipating stage of the storm, most of the particle fountains are older and characterized by weakly buoyant spreading bubbles at mid- and upper levels and downdraft parcels associated with precipitation at lower levels. The spreading updraft parcels congregate at mid- and upper levels and involve more of the air in the storm aloft in a gentle upward motion (as discussed in section 4). The initial introduction of particles aloft and their lateral spread can happen quickly with the action of a few particle fountains. Stratiform precipitation occurs when the updrafts are too weak to support precipitation-sized ice particles (YH Part I, section 2). Since most of the area of the storm is covered by weak vertical velocity (Fig. 3, YH Part II), the ensemble microphysical properties of the storm quickly take on stratiform tendencies (such as the diagonalization of the CFAD of reflectivity, YH Part II, section 3b) even though the storm contains a few very strong updrafts and downdrafts. In contrast, only as the ensemble of particle fountains throughout the storm weaken can the vertical velocity structure begin to take on a stratiform-like appearance. The characteristic stratiform kinematic structure of a volume filled with weak updrafts above the 0°C level and weak downdrafts below begins to be apparent when the majority of particle fountains within the storm are older, weaker, and wider and thus involve more of the volume of the air in the storm. Thus, the apparent lag in the evolution between the microphysics and the kinematics in the storm is a result of the time difference between when the ensemble of particle fountains is first vigorously spreading particles, which occurs in the convective stage of the storm, and when the ensemble of particle fountains is older and primarily serving as an environment conducive to the growth of the previously spread particles, which occurs later in the storm's development.

6. Conclusions

In this three-part study, the ensemble kinematics and microphysics represented by the CFADs of reflectivity, vertical velocity, vertical mass transport, horizontal divergence, and differential reflectivity, in conjunction with mean-value profiles and cross sections, have allowed us to characterize the internal complexity of a multicellular thunderstorm more comprehensively than mean-value profiles and cross sections alone. This more statistical method of characterizing the observations enables us to see order in the complexity and to establish that certain aspects of the ensemble updraft and downdraft behavior can be interpreted in terms of populations of parcels behaving like buoyant bubbles. In particular, it has allowed us to extend the bubble-based conceptual model of updrafts to describe the transition of the storm from a convective toward a more stratiform state.

The more numerous weak and moderate upward and downward velocities (approximately $-5\ \mathrm{m\ s^{-1}} < w < 5\ \mathrm{m\ s^{-1}}$), not the few strongest, accomplished most of the vertical mass transport in the storm (Fig. 3). Therefore, condensation occurred primarily outside the areas of intense upward motion. Most of the mass of water was condensed where ice particles (generated within strong updrafts and subsequently spread laterally as parcels slowed down at upper levels) fell within an environment of weak vertical velocity—a stratiform-like microphysical characteristic (YH Part II, section 3).

As the storm matured from convective to stratiform stages, there was a general weakening of the stronger updrafts and downdrafts, and thus a narrowing of the frequency distribution of the updrafts and downdrafts to about zero (Fig. 3, YH Part II). Concurrent with these changes in vertical velocity distribution at each level, the vertical-mass-transport-weighted CFADs of vertical velocity indicated a change in the vertical distribution of upward-moving air (Fig. 8). Downward mass transport remained concentrated at lower levels throughout the life cycle of the storm (Fig. 3).

The area of upward-moving air was concentrated at low levels in the earlier stages of the storm and became concentrated at mid- and upper levels in the later stages of the storm (Fig. 8). The change in the vertical distribution of upward velocities was related to the behavior of air parcels rising within the storm. The mean mass divergence profiles associated with updrafts showed divergence from 4 to 5 km upward, indicating that above 4–5 km in altitude there was a net deposition of mass of air contributed by updrafts. The slowing and stopping of parcels and associated divergence of the ensemble of updraft parcels indicated that entrainment of environmental air was occurring along the parcels' trajectories and that most of the updraft parcels evidently did not reach the top of the storm.

The convective-to-stratiform transition (e.g., Fig. 1) can be explained by extending bubble-based concep-

tual models of convection. A conceptual model called a particle fountain—consisting of an organization of an updraft behaving like a buoyant bubble and its associated hydrometeors—was devised to incorporate inferences from both the microphysical and kinematic observations (Figs. 12–15). Unlike earlier bubble models, which explain the growing, convective stage of a storm (Scorer and Ludlam 1953; Raymond and Blyth 1986), the particle fountain concept also accounts for the transition of the storm into its stratiform phase and incorporates the basic tenets of microphysical conceptual models of cumulonimbus and stratiform clouds (Hobbs and Rangno 1985).

The manner in which particle fountains explain the convective-to-stratiform transition accounts for the apparent faster evolution toward a stratiform-like state of the ensemble microphysical characteristics of the storm compared to the ensemble kinematic characteristics of the storm. As an updraft parcel rises, associated hydrometeors in the parcel, which are too heavy to suspend, fall through the updraft. When the updraft parcel weakens, slows, and expands (diverges) horizontally, it laterally spreads its load of lighter hydrometeors. These precipitation-size hydrometeors then fall in an environment of predominantly weak vertical velocities and grow in the manner of stratiform precipitation, even while the storm is convectively active. The increasing numbers of particles falling in an environment of weak vertical velocity gave the storm a progressively stronger stratiform-like microphysical character—a trend that became evident with the diagonalization of the topography of the CFADs of reflectivity in the early convective stages of the storm's lifetime and, as the storm aged, became more pronounced approaching the purely stratiform structure exemplified by Fig. 8 of YH Part II.

The particle fountains further explain how the convective kinematic properties of the storm are transformed into a stratiform structure. In the early stages of the storm, bubbles of buoyant air are concentrated at low levels (most of upward mass transport is at low levels). As the storm evolves, production of bubbles at lower levels decreases, and existing bubbles—remnants of previous updrafts—rise through the storm and congregate at mid- and upper levels where they expand (as a result of lowered pressure and entrainment) as they slow and stop. Upward mass transport becomes concentrated at higher levels and a majority of the volume of the storm at mid- and upper levels is thus occupied by weak updraft remnants (Fig. 4, YH Part II and Fig. 3).

The congregation of the smaller-scale, weakly buoyant, spreading updraft parcels involved progressively more of the volume of the storm at mid- and upper levels in a gentle upward motion. Thus, what started as a few locally concentrated particle fountains within a small area of an otherwise quiescent fluid evolved into weak upward motion over wide areas within the storm. As the storm matured, progressively more of the volume of the storm at low levels was occupied by slowly downward-moving air and progressively more of the volume at upper levels was occupied by slowly upward-moving air.

The combination of congregating, weakening, and widening updraft parcels at mid- and upper levels and precipitation-associated downdrafts at lower levels created the stratiform stage signature of a mean vertical velocity profile with weak mean ascent above the 0°C level and weak mean descent below (Fig. 2b). The rigorous, statistical view provided by the CFADs shows that this mean stratiform vertical velocity profile is the combined result of the ensemble of smaller-scale updrafts and downdrafts present at each level.

The analyses of observational data presented in this study advocate a paradigm shift in our thinking about convection. Although the few regions of strongest vertical motion play a part in the overall storm evolution by dispersing particles, it is the many weaker vertical velocities (<5 m s^{-1}) that are the more important determinants of precipitation processes. The more prevalent weaker vertical velocities in the storm move the majority of the mass of air upward and condense most of the mass of precipitation within the storm. It is important to look at the ensemble properties of the entire storm in order to characterize processes in the entire storm. The velocity profiles of the strongest updrafts and the reflectivity associated with them are not representative of precipitation processes occurring in the storm as a whole.

Acknowledgments. Greatly appreciated are the help and advice of Marcia Baker, Michael Biggerstaff, Scott Braun, Richard Carbone, Peter V. Hobbs, Brian Mapes, John McCarthy, Arthur Rangno, Thomas Seliga, David Short, Bradley Smull, Matthias Steiner, John M. Wallace, James Wilson, Ming-Jen Yang, Robert Rilling, Candace Gudmundson, and David Warren. Kay Dewar drafted some of the figures. This research was supported by NASA Space Grant Fellowship NGT-40011, NASA/EOS Global Change Fellowship NGT-30100, NSF ATM-9101653, NASA NAG5-1599, NSF ATM-9024431, ONR N0014-93-1-1271, and the National Center for Atmospheric Research.

REFERENCES

Battan, L. J., 1973: *Radar Observation of the Atmosphere.* The University of Chicago Press, 324 pp.

Biggerstaff, M. I., and R. A. Houze Jr., 1991: Kinematic and precipitation structure of the 10–11 June 1985 squall line. *Mon. Wea. Rev.*, **119,** 3035–3065.

——, and ——, 1993: Kinematics and microphysics of the transition zone of a midlatitude squall-line system. *J. Atmos. Sci.*, **50,** 3091–3110.

Braun, S. A., and R. A. Houze Jr., 1994: The transition zone and secondary maximum of radar reflectivity behind a midlatitude squall line: Results retrieved from dual-Doppler data. *J. Atmos. Sci.*, **51,** 2733–2755.

Browning, K. A., J. C. Fankhauser, J.-P. Chalon, P. J. Eccles, R. G. Strauch, F. H. Merrem, D. J. Musil, E. L. May, and W. R. Sand, 1976: Structure of an evolving hailstorm. Part V: Synthesis and

implications for hail growth and suppression. *Mon. Wea. Rev.*, **104,** 603–610.

Cunning, J. B., 1986: The Oklahoma–Kansas Preliminary Regional Experiment for STORM-Central. *Bull. Amer. Meteor. Soc.*, **67,** 1478–1486.

Dye, J. E., B. E. Martner, and L. J. Miller, 1983: Dynamical–microphysical evolution of a convective storm in a weakly sheared environment. Part I: Microphysical observations and interpretation. *J. Atmos. Sci.*, **40,** 2083–2096.

Ferrier, B. S., and R. A. Houze Jr., 1989: One-dimensional time-dependent modeling of GATE cumulonimbus convection. *J. Atmos. Sci.*, **46,** 330–352.

Fritsch, J. M., 1975: Cumulus dynamics: Local compensating subsidence and its implications for cumulus parameterization. *Pageoph,* **113,** 851–867.

Fulton, R., and G. M. Heymsfield, 1991: Microphysical and radiative characteristics of convective clouds during COHMEX. *J. Appl. Meteor.*, **30,** 98–116.

Gamache, J. F., and R. A. Houze Jr., 1982: Mesoscale air motions associated with a tropical squall line. *Mon. Wea. Rev.*, **110,** 118–135.

——, and ——, 1985: Further analysis of the composite wind and thermodynamic structure of the 12 September GATE squall line. *Mon. Wea. Rev.*, **113,** 1241–1259.

Hobbs, P. V., and A. L. Rangno, 1985: Ice particle concentrations in clouds. *J. Atmos. Sci.*, **42,** 2523–2549.

Houghton, H. G., 1968: On precipitation mechanisms and their artificial modification. *J. Appl. Meteor.*, **7,** 851–859.

Houze, R. A., Jr., 1977: Structure and dynamics of a tropical squall-line system. *Mon. Wea. Rev.*, **105,** 1540–1567.

——, 1993: *Cloud Dynamics.* Academic Press, 573 pp.

——, and E. N. Rappaport, 1984: Air motions and precipitation structure of an early summer squall line over the eastern tropical Atlantic. *J. Atmos. Sci.*, **41,** 553–574.

Knupp, K. R., 1987: Downdrafts within High Plains cumulonimbi. Part I: General kinematic structure. *J. Atmos. Sci.*, **44,** 987–1008.

——, 1988: Downdrafts within High Plains cumulonimbi. Part II: Dynamics and thermodynamics. *J. Atmos. Sci.*, **45,** 3965–3982.

Leary, C. A., and R. A. Houze Jr., 1979: Melting and evaporation of hydrometeors in precipitation from the anvil clouds of deep tropical convection. *J. Atmos. Sci.*, **36,** 669–679.

Lilly, D. K., 1988: Cirrus outflow dynamics. *J. Atmos. Sci.*, **45,** 1594–1605.

Ludlam, F. H., 1952: The production of showers by the growth of ice particles. *Quart. J. Roy. Meteor. Soc.*, **78,** 543–553.

Mapes, B. E., and R. A. Houze Jr., 1993: An integrated view of the 1987 Australian monsoon and its mesoscale convective systems. II: Vertical structure. *Quart. J. Roy. Meteor. Soc.*, **119,** 733–754.

Rangno, A. L., and P. V. Hobbs, 1991: Ice particle concentrations and precipitation development in small polar maritime cumuliform clouds. *Quart. J. Roy. Meteor. Soc.*, **117,** 207–241.

Raymond, D. J., and A. M. Blyth, 1986: A stochastic mixing model for nonprecipitating cumulus clouds. *J. Atmos. Sci.*, **43,** 2708–2718.

——, and ——, 1989: Precipitation development in a New Mexico thunderstorm. *Quart. J. Roy. Meteor. Soc.*, **115,** 1397–1423.

——, R. Solomon, and A. M. Blyth, 1991: Mass fluxes in New Mexico mountain thunderstorms from radar and aircraft measurements. *Quart. J. Roy. Meteor. Soc.*, **117,** 587–621.

Rutledge, S. A., and R. A. Houze Jr., 1987: A diagnostic modeling study of the trailing stratiform region of a midlatitude squall line. *J. Atmos. Sci.*, **44,** 2640–2656.

——, ——, M. I. Biggerstaff, and T. Matejka, 1988: The Oklahoma–Kansas mesoscale convective system of 10–11 June 1985: precipitation structure and single Doppler radar analysis. *Mon. Wea. Rev.*, **116,** 1409–1430.

Scorer, R. S., and F. H. Ludlam, 1953: Bubble theory of penetrative convection. *Quart. J. Roy. Meteor. Soc.*, **79,** 94–103.

Simpson, J., N. E. Westcott, R. J. Clerman, and R. A. Pielke, 1980: On cumulus mergers. *Arch. Met. Geoph. Biokl., Ser. A.* **29,** 1–40.

Smull, B. F., and R. A. Houze Jr., 1987: Dual-Doppler radar analysis of a midlatitude squall line with a trailing region of stratiform rain. *J. Atmos. Sci.*, **44,** 2128–2148.

Srivastava, R. C., 1985: A simple model of evaporatively driven downdraft application to microburst downdraft. *J. Atmos. Sci.*, **42,** 1004–1023.

——, 1987: A model of intense downdrafts driven by the melting and evaporation of precipitation. *J. Atmos. Sci.*, **44,** 1752–1773.

Tao, W.-K., J. Simpson, and S.-T. Soong, 1987: Statistical properties of a cloud ensemble: A numerical study. *J. Atmos. Sci.*, **44,** 3175–3187.

Warner, J., and J. W. Telford, 1963: Some patterns of convection in the lower atmosphere. *J. Atmos. Sci.*, **20,** 313–318.

Westcott, N. E., 1994: Merging of convective clouds: Cloud initiation, bridging, and subsequent growth. *Mon. Wea. Rev.*, **122,** 780–790.

Yuter, S. E., and R. A. Houze Jr., 1995a: Three-dimensional kinematic and microphysical evolution of Florida cumulonimbus. Part I: Spatial distribution of updrafts, downdrafts, and precipitation. *Mon. Wea. Rev.*, **123,** 1921–1940.

——, and ——, 1995b: Three-dimensional kinematic and microphysical evolution of Florida cumulonimbus. Part II: Frequency distributions of vertical velocity, reflectivity, and differential reflectivity. *Mon. Wea. Rev.*, **123,** 1941–1963.

Zipser, E. J., 1969: The role of organized unsaturated convective downdrafts in the structure and rapid decay of an equatorial disturbance. *J. Appl. Meteor.*, **8,** 799–814.

——, 1977: Mesoscale and convective-scale downdrafts as distinct components of squall-line circulation. *Mon. Wea. Rev.*, **105,** 1568–1589.